

# Characterization of Hierarchically Ordered Porous Materials by Physisorption and Mercury Porosimetry—A Tutorial Review

Carola Schlumberger and Matthias Thommes\*

This paper is devoted to the textural characterization of nanoporous materials with a focus on hierarchically ordered materials such as mesoporous zeolites, which exhibit an interconnected pore network consisting of micro-, meso-, and often macropores. Hierarchically ordered zeolites have the potential to improve various industrial applications for instance in the areas of heterogeneous catalysis, separation, gas, and energy storage. Detailed insights into the pore architecture are important, because they control transport phenomena, diffusional rates, and govern selectivity, e.g. in catalyzed reactions. However, a reliable characterization of such complex pore structures is still a major challenge. Within this context, the application of advanced physisorption methodologies for micro-mesopore analysis is discussed but also the characterization of macroporosity by mercury porosimetry is addressed. Fundamental concepts and recent major advances in understanding the underlying mechanisms are highlighted. In conjunction with selected case studies, it is illustrated how the application of advanced physisorption methodologies allows i) for the determination of reliable surface areas, pore volumes, and pore size distributions and ii) for obtaining information about pore network characteristics. This tutorial offers guidance for an advanced characterization of nanoporous materials by physisorption and mercury intrusion/extrusion.

## 1. Introduction

This tutorial deals with the textural characterization of nanoporous materials with a focus on hierarchically organized materials such as mesoporous zeolites. Hierarchically ordered zeolites, which exhibit an interconnected pore network offer improved applicative properties (e.g., activity, selectivity, and conversion). However, the structure-property-performance relationships are not sufficiently well understood, that is, particularly the correlation between texture and improved transport

C. Schlumberger, Prof. M. Thommes  
 Institute of Separation Science and Technology  
 Department of Chemical and Bioengineering  
 Friedrich-Alexander-University Erlangen-Nürnberg  
 91058 Erlangen, Germany  
 E-mail: matthias.thommes@fau.de

 The ORCID identification number(s) for the author(s) of this article can be found under <https://doi.org/10.1002/admi.202002181>.

© 2021 The Authors. Advanced Materials Interfaces published by Wiley-VCH GmbH. This is an open access article under the terms of the Creative Commons Attribution-NonCommercial-NoDerivs License, which permits use and distribution in any medium, provided the original work is properly cited, the use is non-commercial and no modifications or adaptations are made.

DOI: [10.1002/admi.202002181](https://doi.org/10.1002/admi.202002181)

properties (compared to conventional zeolites) is still under investigation.<sup>[1,2]</sup> Hence, detailed insights into the pore architecture are particularly important, but a reliable characterization of such complex pore structures can still be considered a major challenge.

In order to arrive at a comprehensive textural characterization of such hierarchical materials, a combination of complimentary experimental techniques is necessary, for example, gas adsorption, X-ray diffraction (XRD), small angle X-ray and neutron scattering (SAXS and SANS), mercury porosimetry, electron microscopy (scanning and transmission), thermoporometry, nuclear magnetic resonance (NMR) methods, positronium annihilation lifetime spectroscopy (PALS), and electron tomography.<sup>[3–7]</sup> An overview of the different methods for pore size characterization and their application range is given in ref. [8]. Figure 1 illustrates the application ranges of these textural characterization methodologies for pore size analysis, that is, each method offers a limited

length scale of applicability for pore size analysis. Gas adsorption is still the most popular one because it allows assessing the complete range of micro- (pore width < 2 nm), meso- (pore width: 2–50 nm), and to some extend even macropores (pore width > 50 nm). In addition to gas adsorption, mercury porosimetry is used for the characterization of larger nanopores and macropores up to 400 μm. Hence, the combination of gas adsorption and mercury porosimetry allows one to obtain pore structure information over a wide range from pore widths < 4 nm up to at least ≈400 μm, highlighting the importance of these techniques for porous materials characterization.

The physisorption characterization of porous materials using gas adsorption is well established with over a century of dedicated research and development. The basis for our understanding of gas adsorption phenomena and its application for textural characterization were built with the pioneering experimental and theoretical work in the early 20th century.<sup>[10]</sup>

However, during the last 20–30 years, advances in material synthesis allowed for the development of nanoporous materials with tailor made pore structures such as mesoporous molecular sieves and carbon nanotubes.<sup>[11,12]</sup> Using these materials as model materials further enhanced the understanding of adsorption phenomena and the usage of gas adsorption for textural characterization. In addition, the introduction of hierarchical

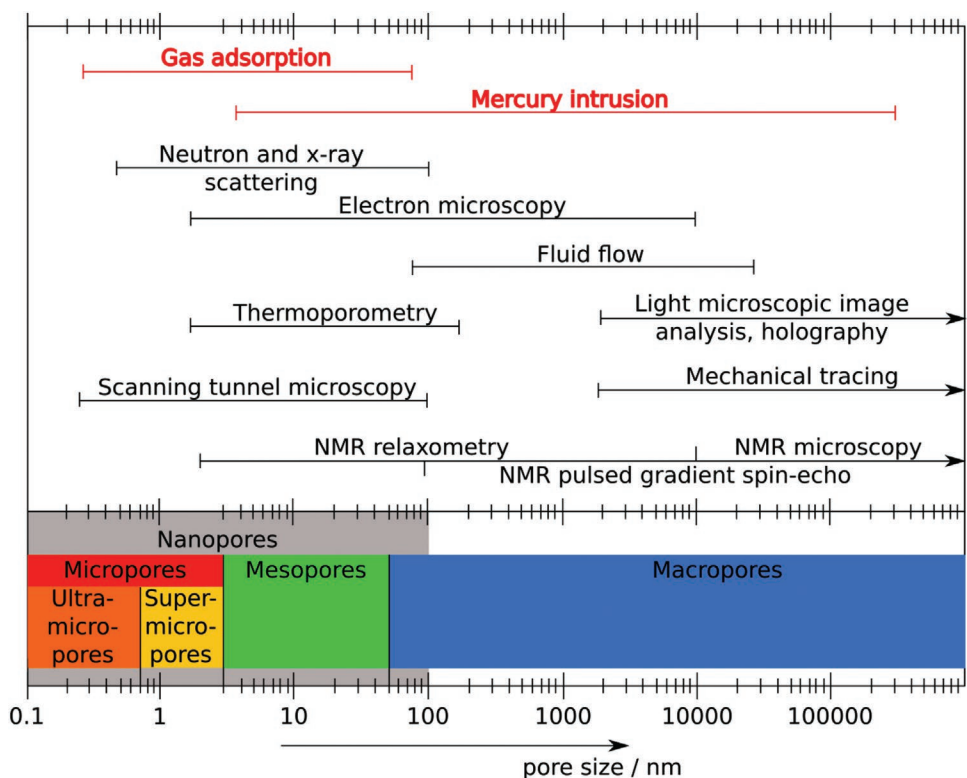


**Figure 1.** Textural characterization methodologies and their typical application ranges for pore size analysis. Based on ref. [9].

pore systems in materials such as zeolites may improve adsorption based applications, for example, catalysis,<sup>[13–20]</sup> gas storage, and separation processes.<sup>[21–28]</sup> The development and application of these novel materials requires the advancement of existing experimental textural characterization protocols. Within this context the major progress in physisorption characterization is strongly interlinked with the development and application of microscopic approaches such as density functional theory (DFT) of inhomogeneous fluids and methods based on molecular simulation, coupled with the refinement of high-resolution experimental protocols and related experimental advances.

The theoretical background of physical adsorption and its significance for textural characterization has been reviewed and described in various textbooks, e.g., refs. [10,29–38]. The application of proper theoretical models, which correctly describe the underlying adsorption mechanism is essential for the determination of surface area, pore size, and pore volume from physisorption isotherms. It has been demonstrated that the application of DFT based approaches (e.g., nonlocal DFT, NLDFT) and molecular simulation methods on high-resolution experimental adsorption isotherms provides a much more accurate and comprehensive pore size analysis compared to classical, macroscopic methods (e.g., Kelvin equation based approaches such as the Barrett–Joyner–Halenda (BJH) method). With these advanced methods it is now possible to obtain an accurate pore size distribution over the wide range of micro- and mesopores, which is crucial for the pore size characterization of hierarchically organized materials. The key results of these advances and corresponding recommendations for a

reliable application of gas adsorption techniques for material characterization have been summarized in a widely accepted report of IUPAC (International Union for Pure and Applied Chemistry).<sup>[39]</sup>

Application of characterization techniques to hierarchical organized nanoporous materials has revealed new phenomena such as cavitation processes during desorption. In order to take this into account, advanced adsorption methodologies have been developed, which are based for instance on a detailed analysis of the hysteresis loop (e.g., hysteresis scanning) or the combination of various adsorptives at various temperatures, coupled with dedicated methods based on DFT or molecular simulation. This allows one to differentiate between different types of interconnected pore networks and to quantify the accessible pore volume.

However, despite this progress, there are still limitations and challenges with regard to assessing the full pore network of a hierarchically structured porous material by gas adsorption alone. For this, a combination of advanced physisorption experiments with complementary techniques, including methods based on digital image analysis, in situ X-ray and neutron scattering, NMR-cryoporometry, and mercury porosimetry is needed. In fact, major challenges are still associated with the assessment of macroporosity. An overview of various techniques for macropore analysis, including liquid intrusion methods such as contact porosimetry, capillary flow porometry, and mercury porosimetry had been given by IUPAC in 2012.<sup>[40]</sup> However, to date, mercury porosimetry is still considered to be the state of the art method for textural analysis of macroporosity.<sup>[40]</sup> In contrast to physical adsorption of fluids such as

nitrogen and argon at their boiling temperatures (i.e., 77 and 87 K, respectively), where the adsorbed phase completely wets the pore walls, liquid metals such as mercury do not wet the majority of materials at or close to room temperature. Therefore, (hydrostatic) pressure must be applied to force mercury into pores. In recent years, a more detailed understanding of the phase behavior of mercury in nanoconfinement has been achieved, which led to advances in the application of mercury porosimetry for meso- and macropore analysis.<sup>[41–43]</sup>

Within this context, we focus in this tutorial mainly on the application of advanced physisorption methodologies for micro-mesopore analysis but also address the characterization of macropores by mercury porosimetry. It needs to be clearly stated that we are not attempting to provide a general review of the adsorption and characterization literature; in fact an extensive review concerning the textural characterization of hierarchically ordered materials had been recently given in ref. [38]. Instead, we rather focus here on providing some practical guidance for the advanced textural characterization of nanoporous and hierarchically structured materials. For this, we first discuss important general concepts of physical adsorption as well as some selected, experimental aspects. In the following, we focus on surface area assessment as well as pore size/volume and network analysis and the necessary understanding of the underlying mechanisms associated with the adsorption, phase, and hysteresis behavior in pores. The different aspects of textural characterization are demonstrated in a case study using mesostructured zeolite Y.<sup>[44]</sup> In addition, we highlight, as already indicated, recent advances in understanding the underlying mechanisms of mercury intrusion/extrusion and correspondent opportunities for advancing macropore analysis.

## 2. Physical Adsorption—General Aspects

Understanding the principles of gas adsorption phenomena and how these phenomena are related to structural properties is essential for reliable textural characterization based on physisorption. Physisorption occurs when an adsorbing gas (adsorptive) is brought into contact with the surface of a solid (the adsorbent). The density of gas molecules increases near the surface due to van der Waals forces. The adsorbed gas molecules within the space of increased density are referred to as the adsorbate. More details on the terminology of gas adsorption can be found in the 2015 IUPAC technical report.<sup>[39]</sup> Some important definitions used during the textural characterization of porous solids are given in Table 1.

Adsorption data are often acquired in form of adsorption isotherms, that is, the adsorbed amount is recorded as a function of pressure of the adsorptive at constant temperature. For subcritical isotherms, one usually plots the adsorbed amount against the relative pressure  $p/p_0$  (with the saturation pressure  $p_0$  of the bulk fluid). However, it should be noted that the term adsorption isotherm is usually used in a way that both adsorption and desorption branches are included in this term, although adsorption describes the onward process of adsorption, while desorption denotes the converse process, in which the adsorbed amount progressively decreases. Adsorption

**Table 1.** Definition of important terms used during textural characterization of porous solids.

|                           | Definition                                                                                                      |
|---------------------------|-----------------------------------------------------------------------------------------------------------------|
| Porous solid              | Solid with cavities or channels that are deeper than they are wide                                              |
| Open pore                 | Cavity or channel with access to the surface                                                                    |
| Interconnected pore       | Pore that communicates with other pores                                                                         |
| Blind pore/deadend pore   | Pore with a single connection to the surface                                                                    |
| Closed pore               | Cavity not connected to the surface                                                                             |
| Nanopore                  | Pore width $\leq 100$ nm                                                                                        |
| Macropore                 | Pore width $> 50$ nm                                                                                            |
| Mesopore                  | Pore width 2–50 nm                                                                                              |
| Micropore                 | Pore width $< 2$ nm                                                                                             |
| Ultramicropore            | Pore width $< 0.7$ nm                                                                                           |
| Supermicropore            | 0.7 nm $<$ pore width $< 2$ nm                                                                                  |
| Pore volume               | Volume of pores (determined by stated method)                                                                   |
| Porosity                  | Ratio of pore volume to overall volume of particle or granule                                                   |
| Surface area              | Area of total surface (determined by stated method)                                                             |
| Internal surface area     | Area of pore walls                                                                                              |
| External surface area     | Area of surface outside all pores or all micropores                                                             |
| Pore size                 | Pore width, that is, diameter in cylindrical pore or distance between opposite walls of slit pore               |
| Adsorbate                 | Adsorbed gas                                                                                                    |
| Adsorptive                | Gas or vapor to be adsorbed                                                                                     |
| Adsorbent                 | Solid material on which adsorption occurs                                                                       |
| Adsorbed amount           | Number of moles of gas adsorbed at a given pressure $p$ and temperature $T$                                     |
| Relative pressure         | Ratio of the equilibrium adsorption pressure $p$ to the saturation vapor pressure $p_0$ at analysis temperature |
| Saturation vapor pressure | Vapor pressure of the bulk liquefied adsorptive $p_0$ at the temperature of adsorption                          |

hysteresis arises when adsorption and desorption curves do not coincide.

The shape of the adsorption isotherm of pure fluids on planar surfaces and porous materials depends on the interplay between the strength of fluid–wall and fluid–fluid interactions coupled with confinement effects caused by the adsorbent's pore structure. Within this context, it is possible to arrive at a classification of characteristic isotherm types, which was recently updated by the IUPAC as shown in Figure 2.<sup>[39]</sup>

Type I isotherms are typical for microporous adsorbents, for example, zeolites and some activated carbons. The uptake of Type I isotherms is limited by the accessible micropore volume of the material. The steep uptake at very low relative pressures is caused by the enhanced attractive adsorptive–adsorbent interactions in narrow micropores. The filling of narrow micropores, that is, ultramicropores of width  $< 0.7$  nm with adsorptives such as nitrogen and argon at 77 and 87 K, respectively, gives rise to Type I(a) isotherms while Type I(b) isotherms are found for materials exhibiting a wider pore size distribution including supermicropores and narrow mesopores (less than  $\approx 2.5$  nm).

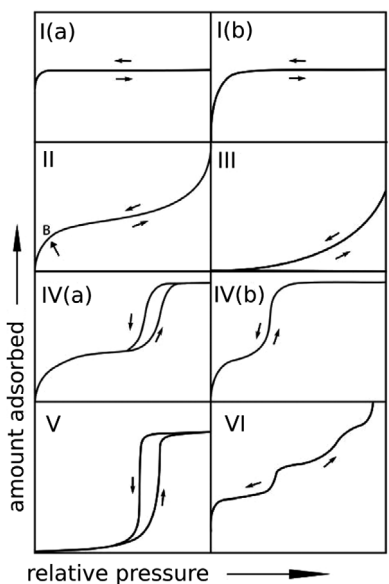


**Figure 2.** IUPAC classification of physisorption isotherms. Reproduced with permission.<sup>[39]</sup> Copyright 2015, De Gruyter.

Physisorption on nonporous and macroporous materials with heterogeneous surfaces leads to Type II isotherms. Unrestricted monolayer–multilayer formation is possible up to high relative pressures during the adsorption process. In contrast, highly uniform nonporous materials show a layer by layer adsorption leading to a Type VI isotherm. This can be observed for example for argon and krypton adsorption on graphitized carbon blacks.<sup>[10]</sup>

If the fluid–wall interactions are relatively weak and the adsorbate is not completely wetting the surface, a Type III isotherm occurs. Due to stronger interactions between fluid

molecules compared to the fluid–wall interactions, the molecules build clusters around preferred sites of the adsorbent. The shape of Type V isotherms is similar to the shape of Type III isotherms in the low relative pressure range. This is also caused by relatively weak fluid–wall interactions. For Type V isotherms, the molecular clustering is followed by pore filling accompanied by hysteresis. Type V isotherms are for instance observed for water adsorption on hydrophobic micro- and mesoporous adsorbents.

Type IV isotherms are typical for mesoporous materials (e.g., mesoporous molecular sieves). For these materials, the monolayer–multilayer formation is followed by pore condensation which means that the gas condenses to a liquid-like state in a pore at a pressure less than the saturation pressure  $p_0$  of the bulk liquid.<sup>[32,33]</sup> Type IV isotherms finally reach a saturation plateau. Type IV(a) isotherms with hysteresis can be distinguished from Type IV(b) isotherms without hysteresis. Hysteresis occurs when the pore width exceeds a certain critical width which is depending on the adsorptive and temperature. For nitrogen and argon at 77 and 87 K, respectively, hysteresis occurs for pores larger than  $\approx 4$  nm.<sup>[30,32,45]</sup> In contrast, adsorbents having smaller mesopores show a completely reversible adsorption behavior leading to a Type IV(b) isotherm.

The occurrence of hysteresis loops associated with pore condensation can be attributed to adsorption metastability, but there are additional contributions originating from pore network effects, which also affect the shape of the hysteresis loops (details of the origin of hysteresis are discussed in Section 5.2). Hence, there is a correlation between the shape of the hysteresis loop and the texture of the adsorbent. An empirical classification of hysteresis loops in five different types (H1, H2(a), H2(b), H3, H4, and H5) was recently given by IUPAC<sup>[39]</sup> as illustrated in **Figure 3**. These different types of hysteresis and their correlation with the underlying adsorption mechanisms and pore structure will be discussed in more detail in Section 5.2.

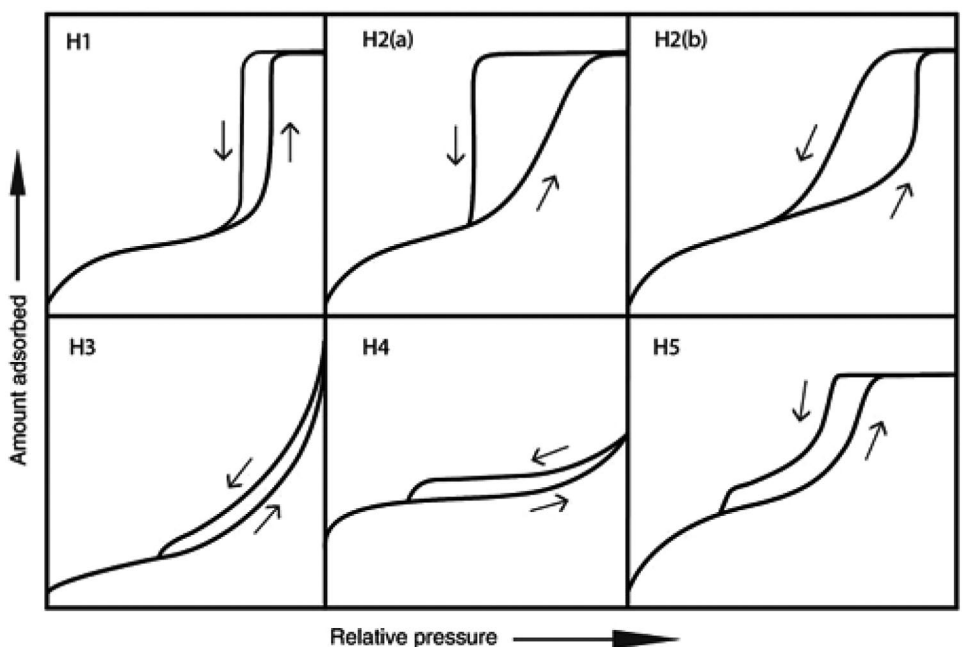


**Figure 3.** IUPAC classification of hysteresis loops. Reproduced with permission.<sup>[39]</sup> Copyright 2015, De Gruyter.

### 3. Experimental Aspects

#### 3.1. General

The adsorbed amount can be obtained by manometric (volumetric) and gravimetric methods, carrier gas and calorimetric techniques, nuclear resonance, as well as by a combination of calorimetric and impedance spectroscopic measurements.<sup>[46–48]</sup> However, the most frequently used methods for physical adsorption analysis are the volumetric (manometric) and gravimetric methods. The gravimetric method, which is based on a sensitive microbalance, is convenient to use for the study of adsorption not too far from room temperature and is considered the most accurate experimental method for adsorption measurements including vapors (e.g., water, benzene, and toluol). However, the adsorbent is not in direct contact with the thermostat which leads to problems with assessing the exact temperature of the adsorbent, particularly if experiments are performed at cryogenic temperatures such as the boiling temperature of nitrogen and argon (77 and 87 K, respectively), which are primarily used for surface area and pore size characterization. The standard technique for such experiments is the manometric technique, which is based on calibrated volumes and pressure measurements and uses the general gas equation of state. An important requirement is that the adsorbed amount is calculated by determining the difference of the total amount of gas admitted to the sample cell with the adsorbent and the amount of gas in the dead space. Experimental details of the manometric method are described in various textbooks; hence, we do not discuss these details within the scope of this article.<sup>[8,10,30,31,37,39,49]</sup>

Determination of surface area, pore size, and volume of mesoporous materials requires instruments which are capable of measuring isotherms in a moderate pressure range ( $p/p_0 = 0.05\text{--}0.99$ ). However, adsorption in microporous adsorbents can span a broad spectrum of pressures (up to seven orders of magnitude). Hence, special care is necessary for the pressure measurements. Consequently, more than one pressure transducer is necessary to measure all equilibrium pressures with sufficient accuracy.

Characterization of materials containing micropores requires the measurement at very low relative pressure (to  $p/p_0 = 10^{-7}$ ). Hence, efficient turbomolecular vacuum pumping systems and low-pressure transducers are necessary in this case. For a sufficiently high accuracy, it is therefore desirable to use a combination of different transducers with maximum ranges of < 0.133 kPa (1 Torr), 1.33 kPa (10 Torr), and 133 kPa (1 000 Torr).

The knowledge of the dead space, that is, effective void volume, is essential when measuring adsorption with manometric techniques. Usually, a non-adsorbing gas, that is, helium is often used to determine the dead space during the adsorption measurement. However, the use of helium may be restricted<sup>[30,37,50]</sup> as the entrapment of helium at cryogenic temperatures is possible in narrow micropores. Hence, the shape of the adsorption isotherm in the ultra-low pressure range may be significantly affected if helium is not properly removed prior to analysis.<sup>[39]</sup> Therefore, after exposure of the sample to helium during free space measurements, it is highly recommended to evacuate the sample cell and repeat degassing of the sample

at elevated temperatures (this so-called He-removal procedure should be performed at least at room temperature) before continuing with analysis. Another possibility is to determine the void volume with helium after completion of the sorption measurement.

For some materials exhibiting extremely narrow ultramicropores (such as some zeolites, and activated carbon), it is beneficial to avoid the use of helium because—in contrast to helium—the entry of nitrogen and argon is restricted due to diffusion limitations. The problem can be addressed performing a procedure which consists of assessing the volume of the empty sample cell with the adsorptive (e.g., argon) followed by the determination of a subsequent calibration curve (again with the empty sample cell) under the same operational conditions as the adsorption measurement. The actual sample volume can then be calculated using the calibration curve and the sample density (skeletal density).<sup>[39]</sup>

Another complication associated with ultralow pressure measurements is that for gas pressures below ≈80–100 millitorr (i.e.,  $p/p_0 < 10^{-4}$  for nitrogen and argon adsorption at 77 and 87 K, respectively) pressure differences along the capillary of the sample bulb on account of the Knudsen effect have to be taken into account (i.e., thermal transpiration correction). Thermal transpiration results in a pressure gradient between the sample, which is kept at the (cryogenic) measurement temperature, and the pressure transducer, which is at room temperature, if the inner diameter of the tubing between the two parts of the system is very small compared with the mean free path of the gas. This causes significant pressure measurement errors if not properly corrected.<sup>[39,51,52]</sup> Hence, a thermal transpiration correction must be applied in order to obtain accurate data during the characterization of materials containing ultramicropores.<sup>[39,51,52]</sup>

To ensure high accuracy and reproducibility of the measurement, the saturation pressure  $p_0$  should be recorded during the measurement for every datum point, accurate  $p_0$  pressure information is particularly important for an accurate pore size analysis of materials exhibiting large mesopores, where pore condensation occurs close to the saturation pressure. Additionally, the purity of the adsorptive should not be less than 99.999%.<sup>[39]</sup>

To verify the validity of the measurement results and the apparatus performance a proper certified reference material should be tested on a regular basis to monitor instrument calibration and performance. Certified reference materials are offered for instance by the National Institute of Standards and Technology (NIST) or the German Federal Institute for Materials Research and Testing (BAM), Institute for Reference Materials and Measurements (IRMM) at Geel, Belgium, and others.

#### 3.2. Sample Preparation

Prior to the adsorption experiment, it is required to remove all physically adsorbed material from the adsorbent surface while avoiding irreversible changes to the surface. In principle, this can be accomplished by vacuum pumping or purging with an inert gas at elevated temperatures.<sup>[30,37,39]</sup> Particularly for microporous materials, for example, for zeolites, outgassing under vacuum is desirable as the adsorption measurements

often start at relative pressures as low as  $10^{-7}$ . This can again be achieved by using a turbomolecular pump, which, if coupled with a diaphragm roughing pump, allows the sample to be outgassed even in a completely oil free system.

Well-defined outgassing protocols are often available for known materials. In case of unknown samples, the maximum temperature for outgassing should be determined using thermogravimetric analysis, spectroscopic methods, or trial experiments using different degassing conditions of time and temperature.<sup>[39,49]</sup>

A pressure-controlled procedure with a dedicated heating program is recommended for sensitive samples. In this case, the heating rate is varied depending on the pressure during the degassing process. Degassing of the sample and hence, removal of adsorbed molecules can induce an increase in pressure. If the pressure increase is higher than a specified value, increasing of the temperature is stopped until the pressure falls below the limit. This procedure can help to avoid structural changes in microporous materials due to fast heating rates. Additionally, this method can help to prevent sample elutriation during the outgassing process.

Outgassing time and temperature as well as the residual pressure should be carefully controlled and recorded to ensure reproducibility of the experiments. A constant mass or constant pressure for a period of 15 to 30 min indicates that the removal of adsorbed molecules is completed. The mass of the outgassed sample should then be used during the adsorption measurement and for calculation of the specific surface area and pore volume.<sup>[53]</sup>

### 3.3. Choice of Adsorptive

Ideally, for textural characterization, the adsorption isotherm should be considered a fingerprint of the pore structure for textural characterization. Hence, in this case, it is essential to choose an adsorptive, which is not affected in an appreciable way by the surface chemistry. Hence, few interactions between

the adsorptive and (polar) surface sites are desirable. In contrast, investigating the surface chemistry requires adsorptives, for which the isotherm can be considered a fingerprint of the surface chemistry.

This means that the proper choice of adsorptive is crucial for an accurate and comprehensive pore structural analysis. For many years, nitrogen adsorption at 77 K has been generally accepted as the standard method for both micro- and mesopore size analysis. However, by now it is well known that the quadrupole moment of the nitrogen molecule is largely responsible for specific interactions with a variety of surface functional groups and exposed ions. This not only affects the orientation of the adsorbed nitrogen molecule on the adsorbent surface leading to inaccurate results during surface area assessment, but it also strongly affects the micropore filling pressure. Specific interactions with surface functional groups cause the problem that the pore filling pressure is not correlated with the micropore size in a straightforward way. For example, for many zeolites and metal organic framework materials (MOFs), the initial stage of physisorption is shifted to extremely low pressures ( $p/p_0 \approx 10^{-7}$ ) where the rate of diffusion is extremely slow.<sup>[38]</sup> An example of a N<sub>2</sub> isotherm on Faujasite zeolite is shown in Figure 4. Pore filling occurs at low relative pressures ( $p/p_0 < 10^{-5}$ ) and long equilibration times are required due to slow diffusion. Hence, measuring equilibrated adsorption isotherms is difficult in this low relative pressure range.<sup>[29,38]</sup> The effect of the chosen equilibration time is shown in Figure 4. Too short equilibration times lead to under-equilibrated data, and hence, isotherms shift to higher relative pressures. However, on the other hand Figure 4 also clearly reveals that at higher pressures (i.e.,  $p/p_0 > 10^{-5}$ ), both isotherms agree well, that is, the differences in equilibrium criteria do not play here a significant role anymore. Pore filling with argon at 87 K also occurs in this relative pressure range for the Faujasite zeolite as demonstrated in Figure 4. This is because in contrast to nitrogen, argon at 87 K (liquid argon temperature) does not exhibit specific interactions with polar surface functional groups. As a consequence and due to the slightly higher temperature, argon at 87 K fills the micropores

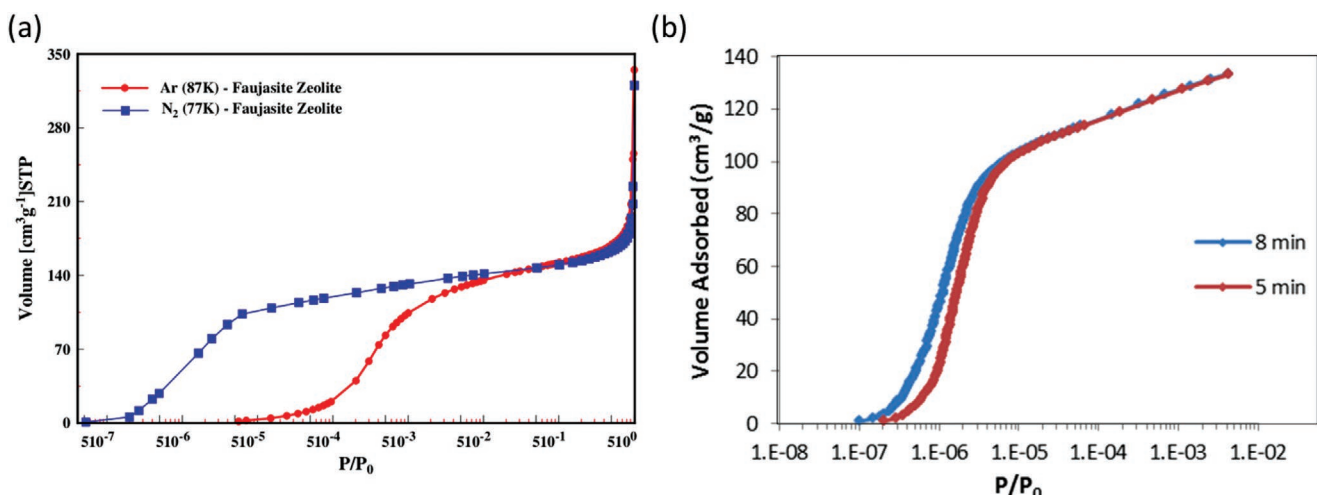


**Figure 4.** a) Ar (87 K) and N<sub>2</sub> (77 K) adsorption isotherm of Faujasite Zeolite (semilog plot). Reproduced with permission.<sup>[32]</sup> Copyright 2014, Springer Nature. b) Effect of equilibration time at low relative pressures on the N<sub>2</sub> adsorption isotherm of Faujasite zeolite. The isotherm is shifted to higher relative pressures in case of under-equilibration.

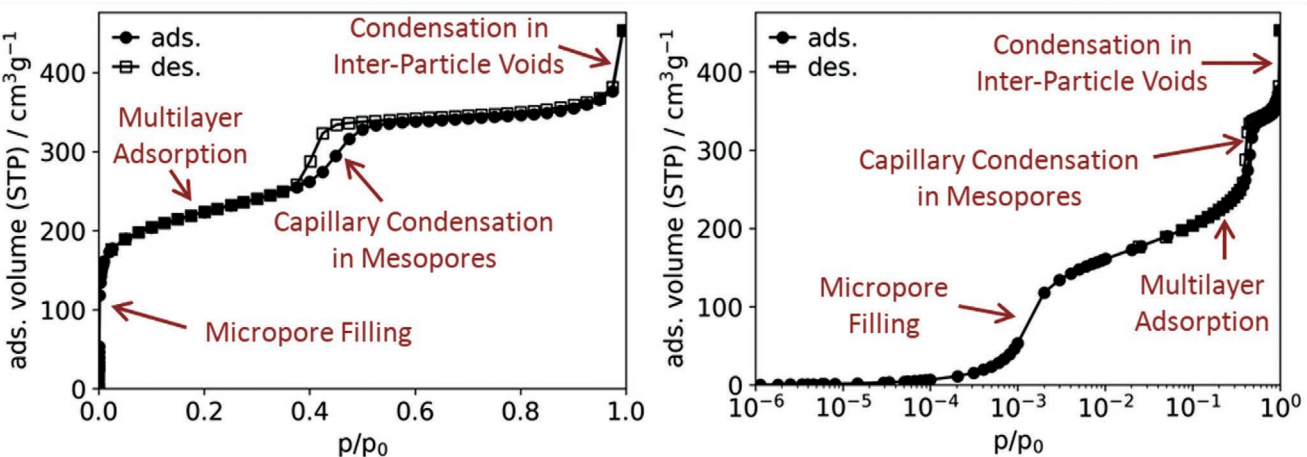


Figure 5. Linear (left) and semi-logarithmic (right) plot of the Ar (87 K) isotherm on mesoporous, hierarchically ordered zeolite Y.<sup>[53]</sup>

of dimensions 0.5–1 nm as present in materials exhibiting polar surface functionality such as zeolites and MOFs at significantly higher relative pressures compared to nitrogen at 77 K, leading to accelerated diffusion and faster equilibration time.

It has been demonstrated, that argon adsorption at 87 K allows to resolve small differences in pore size with a resolution of at least 0.1 nm.<sup>[54,55]</sup> Hence, for all the above discussed reasons, argon adsorption at 87 K is now recommended by IUPAC for pore size analysis, particularly for micropore size analysis of materials which exhibit polar surface functionality.<sup>[39]</sup> Within this context it should be noted that it is now possible to achieve liquid argon temperature by using commercially available cryo-coolers or simple cryostats.

An example of argon (87 K) adsorption on mesoporous structured zeolite Y is shown in Figure 5. The shape of the isotherm is a reflection of the micro-mesoporous structure of the adsorbent. Please note that in order to reveal the details in the low pressure region where micropore filling occurs, the isotherm is also displayed in a semi-logarithmic scale of relative pressures (see Figure 5 right), while details of mesoporosity and the associated hysteresis loop are best visible in the linear display.

However, because of kinetic restrictions at cryogenic temperatures (87 and 77 K), argon and nitrogen adsorption is of limited value for the characterization if the porous materials exhibits narrow micropores. The use of CO<sub>2</sub> at temperatures close to 273 K was suggested to address this problem. In this case, diffusion rates are enhanced due to the slightly smaller kinetic diameter and the high temperature leading to a better resolution of ultramicropores.<sup>[10,45,56–58]</sup> However, caution has to be applied for materials with polar surface functionality, which prohibits the use of CO<sub>2</sub> for reliable pore size analysis for zeolites and MOFs due to the even stronger quadrupole moment of CO<sub>2</sub> compared to N<sub>2</sub>.

On the other hand, CO<sub>2</sub> adsorption can still be useful for assessing the pore volume/porosity for materials, which have pores, which cannot be assessed by nitrogen or argon. This has been demonstrated for a series of type A zeolites.<sup>[59]</sup> The pore size in zeolite NaA is ≈0.4 nm and the results of the study confirm that N<sub>2</sub> molecules cannot enter the pores. However, useful CO<sub>2</sub> adsorption isotherms at 273 K could be obtained on

zeolite NaA and the micropore volume calculated from the CO<sub>2</sub> adsorption data was found to be in good agreement with the values obtained from XRD. Thus, it needs to be stressed that while CO<sub>2</sub> adsorption cannot be utilized for pore size analysis of materials with polar surface functionality, reliable information about the volume of narrow micropores can still be obtained.

#### 4. Surface Area Assessment

The standard method applied in physical adsorption characterization for surface area assessment is the BET (Brunauer, Emmett, and Teller) method and it continues to be the most widely used procedure for evaluating the surface area of porous and finely-divided materials, in spite of the weakness of its well-known shortcomings.<sup>[10,30,60]</sup> Indeed, under certain, carefully controlled conditions, the BET area of a non-porous, macroporous, or mesoporous solid, that is, materials which give rise to a Type II or a Type IV isotherm, can be regarded as the probe accessible area or the effective area available for the adsorption of specified adsorptives. In this case, the isotherm can be converted to the linear “BET plot” and the value of the BET monolayer capacity  $n_m$  is calculated using the BET equation:

$$\frac{\frac{p}{p_0}}{n\left(1-\frac{p}{p_0}\right)} = \frac{1}{n_m C} + \frac{C-1}{n_m C} \left(\frac{p}{p_0}\right) \quad (1)$$

Usually, linear BET plots can be found in the relative pressure range  $p/p_0 = 0.05–0.3$  for Type II and IV(a) isotherms.<sup>[61]</sup> Knowing the cross-sectional area  $\sigma$ , the surface area can subsequently be calculated using the following equation, where  $N_a$  is the Avogadro constant:

$$S = n_m \cdot N_a \cdot \sigma \quad (2)$$

However, the application of the BET method on materials with micropores is not straightforward because it is impossible

to separate the processes of monolayer–multilayer adsorption and micropore filling. Within the same context, the BET method is also inaccurate for mesoporous materials exhibiting Type IV(b) isotherms. In this case, the monolayer–multilayer formation on the pore walls is occurring very close to the pressure range of pore condensation, which can lead to a significant overestimation of the monolayer capacity.

With microporous adsorbents, the linear range of the BET plot, that is, the range of relative pressures where the BET method should be applied, is often narrow and may be difficult to locate. A useful procedure was introduced in ref. [62], which allows one to overcome this difficulty and determine the linear BET range in an unambiguous way. This procedure is essentially based on three criteria: a) The constant  $C$  must be positive, b) the BET equation should only be applied in the region where  $\sqrt{1 - \frac{p}{p_0}}$  is increasing continuously with  $p/p_0$ , and c) the BET monolayer capacity should be in the pressure region selected for the BET plot (for more details please see ref. [60]). However, it should be stressed that the BET area derived from an isotherm obtained on microporous materials must not be treated as a realistic probe accessible surface area but rather as an apparent surface area.

Caution has to be applied if this procedure is used for assessing the BET area of materials containing both micro- and mesopores as surface area assessment is not possible if pore condensation occurs in the pressure range selected.

An example is shown in **Figure 6** which illustrates the determination of the BET area for the mesostructured zeolite Y. The calculation of the BET area is based on the argon (87 K) adsorption isotherm shown in Figure 5.

The upper limit of the BET range can be defined as the maximum point and the linear region of the BET plot can be found from low relative pressures, for example,  $p/p_0 \approx 10^{-4}$ , to the maximum point. A positive constant  $C$  was calculated for the illustrated BET range and the determined monolayer capacity is in the pressure region selected. Additionally, one has to assure that no pore condensation in mesopores is occurring in the selected BET range.

Additionally, the heterogeneous nature of many surfaces can be problematic during surface area determination. As discussed in the previous section, the quadrupole moment of nitrogen causes specific interactions with polar surface sites, for example, hydroxyl groups. This affects the orientation of

the adsorbed nitrogen molecules. Consequently, the effective cross-sectional area can be smaller than the customary value of  $0.162 \text{ nm}^2$ . This affects the accuracy of the BET areas obtained with  $\text{N}_2$  adsorption.

Hence, argon adsorption at 87 K is the recommended adsorptive for surface area assessment as the monatomic argon does not exhibit a quadrupole moment and hence, no specific interactions with surface functional groups occur.<sup>[39]</sup> Therefore, the cross-sectional area ( $0.142 \text{ nm}^2$ ) is less dependent on the properties of the adsorbent surface. Due to its quadrupole moment, nitrogen adsorption can lead to an overestimation of the specific surface area up to 20–25%.<sup>[39,53]</sup>

To summarize, one has to take extreme caution when applying the BET method to materials, which exhibit appreciable amounts of microporosity as can be found in many nanoporous materials such as zeolites, MOFs, active carbons. The obtained BET area (preferably calculated from the argon at 87 K isotherm) can only be considered as an apparent surface area, which may be regarded as a useful adsorbent “fingerprint”.

Other methods to obtain a specific surface area from gas adsorption are based on the application of the standard isotherm concept, for example, t- and alpha-s methods (including the high resolution alpha-s analysis).<sup>[31,63]</sup> By subtracting the external surface area from the BET area, one can determine a micropore surface area. A micropore surface area can also be obtained by methods related to the Dubinin approach (i.e., the Dubinin–Kaganer method), for example, see refs. [10,30,37]. Another alternative to obtain quite accurate surface areas of nanoporous carbons and to differentiate between micro- and external surface area is the application of approaches based on DFT, which calculates the specific cumulative surface area (specific surface area as a function of pore size) over the complete range of micro- and mesopores. However, accurate results are obtained only if the given experimental adsorptive/adsorbent system is compatible with one of the available DFT methods.

## 5. Pore Size and Volume Analysis

### 5.1. Adsorption Mechanism

In order to obtain textural properties such as pore size distribution, pore volume, and other structural information of

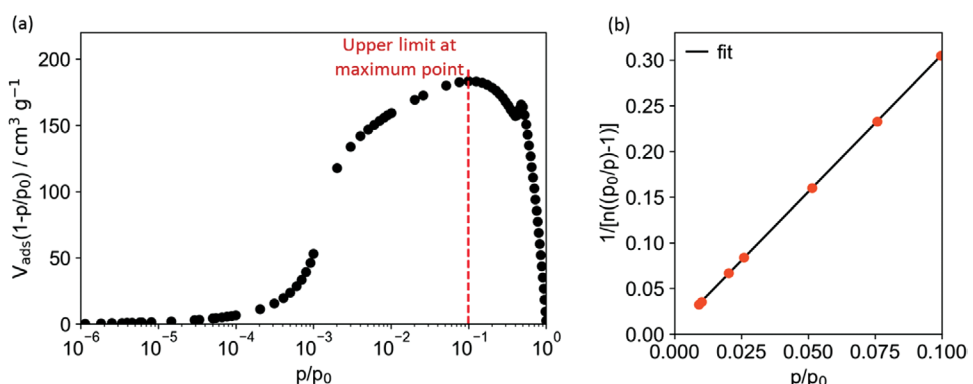


**Figure 6.** Determination of the BET area of mesoporous zeolite Y using Ar (87 K) adsorption. a) Plot of  $V_{\text{ads}}(1 - p/p_0)$  versus  $p/p_0$  for reproducible determination of the linear BET range. b) Linear BET plot.

materials with hierarchical pore structure from the analysis of gas adsorption isotherms it is necessary to understand the underlying, often quite complex, adsorption mechanisms in much detail. The mechanisms of micro- and mesopore filling differ substantially. While micropores fill in a continuous fashion at relative pressures  $< \approx 0.15$  (for N<sub>2</sub> and Ar at 77 and 87 K, respectively), pore filling of mesopores is associated with a shifted vapor–liquid phase transition.

The filling of ultramicropores is entirely governed by the enhanced fluid–solid interactions. However, in addition to the strong adsorption potential, a cooperative mechanism including both fluid–solid interactions and fluid–fluid interactions plays a role in the pore filling process of wider micropores (i.e., supermicropores). The relative pressure at which micropore filling occurs depends essentially on the size and nature of adsorptive molecules, pore shape, and effective pore width.

The sorption behavior in mesopores depends not only on the fluid–wall attraction, but also significantly on the attractive fluid–fluid interactions. This leads to the occurrence of multilayer adsorption and capillary condensation. Pore condensation represents a phenomenon whereby gas condenses to a liquid-like phase in pores at a pressure less than the saturation pressure,  $p_0$ , of the bulk fluid. It represents an example of a shifted bulk transition under the influence of the attractive fluid–wall interactions. Pore condensation is very often accompanied by hysteresis, which is observed in single pores as well as in pore networks.

As already indicated, in case of complete wetting, the pore walls are covered by a multilayer adsorbed film at the onset of pore condensation. The stability of this film is determined by the attractive fluid–wall interactions, the surface tension, and curvature of the liquid–vapor interface. Multilayer adsorption can for instance be described in the spirit of the Frenkel–Halsey–Hill theory (for more details, please see ref. [30]). One of the basic assumptions is that the (sufficiently thick) adsorbed multilayer film can be considered as a slab of liquid, which reveals the same properties (i.e., density) as the bulk liquid would have at this temperature. The only modification to its free energy arises from the interaction with the solid, that is, the adsorption forces (dispersion forces). The film thickness cannot grow unlimited in pores. The stability of the multilayer adsorbed film is determined by the long-range van der Waals interactions, and by the surface tension and curvature of the liquid–vapor interface.

At a certain critical thickness  $t_c$ , pore condensation occurs in the core of the pore, controlled by intermolecular forces in the core fluid. Pore condensation can be described based on the Kelvin equation for pores of uniform shape and width, that is, ideal slit-like or cylindrical mesopores. In this case, the shift of the gas–liquid phase transition of a confined fluid from bulk coexistence is expressed in macroscopic quantities like the surface tension  $\gamma$  of the bulk fluid, the densities of the coexistent liquid  $\rho_l$  and gas  $\rho_g$  (with  $\Delta\rho = \rho_l - \rho_g$ ) and the contact angle  $\theta$  of the liquid meniscus against the pore wall. The modified Kelvin equation<sup>[10,30,37]</sup> is given for cylindrical pores:

$$\ln\left(\frac{p}{p_0}\right) = -\frac{2\cos(\theta)}{RT \Delta\rho (r_p - t_c)} \quad (3)$$

Here,  $R$  is the universal gas constant,  $r_p$  is the pore radius and  $t_c$  is the thickness of an adsorbed multilayer film, which is build prior to pore condensation. A contact angle of 0° (indicating complete wetting of the adsorbate layer) can be assumed for nitrogen and argon adsorption at 77 and 87 K, respectively. However, pore condensation is generally expected to occur at relative pressures  $p/p_0 < 1$  for contact angles smaller than 90°.

The Kelvin equation provides a relationship between the pore diameter and the pore condensation/evaporation pressure, and predicts that pore condensation/evaporation shifts to a higher relative pressure with increasing pore diameter and temperature. The modified Kelvin equation (Equation (3)) takes into account that there exists a preadsorbed multilayer film prior to the onset of pore condensation. Equation (3) serves as the basis for many methods applied for mesopore analysis, including the BJH method,<sup>[64]</sup> which is widely used.

In order to account for the preadsorbed multilayer film, the Kelvin equation is combined with a standard isotherm or a so-called t-curve, which usually refers to adsorption measurements on a non-porous solid. Accordingly, the preadsorbed multilayer film is assessed by the statistical (mean) thickness of an adsorbed film on a nonporous solid of a surface similar to that of the sample under consideration. Such statistical thickness equations were derived for instance by Halsey, Harkins–Jura, and de-Boer.<sup>[10,30]</sup> However, it is obvious that assuming the situation of a nonporous, planar surface for the evaluation of the preadsorbed film thickness cannot be valid anymore in case of narrow pores, where the curvature of the pore walls and their adsorption potential has a pronounced effect on the film thickness and its interfacial tension.

Moreover, the Kelvin equation cannot accurately describe the confinement effect on the state of pore fluid and the origin of hysteresis. More advanced classical approaches such as the Broeckhoff and de Boer theory<sup>[65–67]</sup> and the Saam–Cole approach<sup>[68]</sup> capture essentially the mechanisms of pore condensation and hysteresis.

However, all these thermodynamic, macroscopic theories do not account for the peculiarities of the critical region of a confined fluid. However, a detailed and accurate description of the mechanisms associated with pore condensation and hysteresis is essential for reliable pore size analysis. The corresponding inaccuracy in the pore size analysis is described in Section 5.3. In contrast, microscopic approaches based on statistical mechanics such as DFT, lattice model calculation, and various computer simulation studies (see refs. [39,69,70]) are capable of accurately describing the underlying mechanisms of pore condensation and hysteresis suggesting that a fluid confined to a single pore can exist with two possible density profiles corresponding to inhomogeneous gas- and liquid configurations in the pore. In this sense, pore condensation reflects a first order phase transition between an inhomogeneous gas configuration, which consists of vapor in the core region of the pore in equilibrium with a liquid like adsorbed film and a liquid configuration, where the pore is filled with liquid.<sup>[32,33]</sup> At the pore critical point of the confined fluid (for simplicity assuming here that a fluid is confined in a simple slit-pore), these two hitherto distinct fluid configurations will become indistinguishable, that is, a pore condensation step cannot be observed anymore. The critical temperature of the confined fluid is shifted to lower

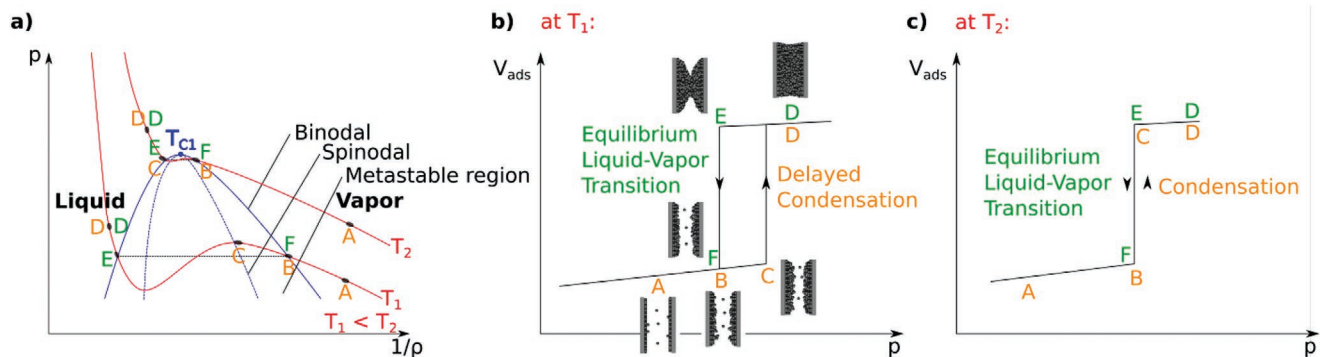


**Figure 7.** a) Adsorption at temperature  $T_1$  and  $T_2$  ( $T_1 < T_2$ ) in a schematic pressure-density phase diagram of a fluid confined in a mesopore. b) Resulting Type IV(a) isotherm at temperature  $T_1$  with marked points A to D during adsorption and D to F during desorption. Insets: Adapted with permission.<sup>[30]</sup> Copyright 2004, Kluwer Academic Publishers. c) Type IV(b) isotherm at temperature  $T_2$  near the pore critical temperature.

temperatures, that is, in contrast to the predictions of the Kelvin equation pore condensation and hysteresis will vanish already at temperatures below  $T_c$ . The shift of the critical temperature can be rationalized by the argument that a fluid in narrow pores is an intermediate between a 3D fluid and a 1D fluid for which no critical point exists at  $T > 0$ . Hence, the shift of the pore critical temperature is correlated with the pore width, that is, the narrower the pore, the lower the pore critical temperature. Consequently, at a given subcritical temperature pore condensation is only possible in pores, which are wider than the critical pore size  $w_c$ . In addition, the effect of confinement on the phase and critical behavior of a confined fluid is important for understanding hysteresis in mesopores, as described in the next section.

## 5.2. Origin of Hysteresis

Understanding the underlying mechanisms associated with pore condensation and hysteresis is crucial for a reliable textural analysis of nanoporous materials exhibiting mesopores. There are various factors contributing to hysteresis and their investigation is still an active field of research. Within the independent (single) pore model, sorption hysteresis is considered an intrinsic property of a vapor–liquid phase transition, reflecting the existence of metastable gas states. The network model of hysteresis describes additional contributions, which effect the desorption branch (i.e., pore evaporation) based on phenomena such as pore blocking/percolation and cavitation.

As already indicated hysteresis may occur because of the existence of a metastable state of the pore fluid associated with the nucleation of liquid bridges.<sup>[30,39,69,70,75]</sup> Figure 7 illustrates this situation in a schematic pressure-density (here displayed as  $1/\rho$ ) phase diagram for a fluid confined in a mesopore at constant temperature  $T_1$  and  $T_2$ , respectively. The phase diagram of the pore fluid is shifted to higher densities as compared to the corresponding bulk phase diagram,<sup>[69,71–74]</sup> but this is not shown here for clarity.

The average density of the pore fluid can be directly correlated with the amount adsorbed. For temperature  $T_1$  a Type IV(a) isotherm is observed as shown in Figure 7b while for  $T_2$  (with  $T_1 < T_2$ ) a Type IV(b) isotherm is obtained (see Figure 7c).

The delay in pore condensation is consistent with the classical van der Waals picture, which predicts that the metastable

adsorption branch terminates at a vapor–liquid spinodal where the limit of stability for the metastable states is achieved and the pore fluid spontaneously condenses into a liquid-like state (so-called spinodal condensation<sup>[70,76]</sup> and references therein). At temperature  $T_1$ , points A to D represent the capillary condensation during adsorption and points D to F the evaporation during desorption. During the adsorption process, crossing the binodal (B) does not induce a phase transition. The delayed phase transition occurs near the spinodal (C). In contrast, the pore is already filled with liquid-like condensate at the beginning of the desorption process. The liquid–vapor interface with the bulk vapor phase leads to evaporation without nucleation via a receding meniscus.<sup>[45]</sup> Hence, crossing the binodal (E) induces the phase transition. Therefore, the desorption process is associated with the equilibrium liquid–vapor transition.

Increasing the temperature leads to a reduction of the metastable width and hence, to a decreasing hysteresis width. Hysteresis should disappear at the pore critical temperature.<sup>[71,77]</sup> However, experimental hysteresis already disappears at a temperature near the pore critical temperature,<sup>[69,70,77,78]</sup> which is defined as hysteresis critical temperature.<sup>[77]</sup> This is the case at temperature  $T_2$ , which is above the hysteresis critical temperature in Figure 7. In this case, fluctuations are sufficient to overcome the now very small nucleation barrier associated with the width of the metastable region. Hence, pore condensation already occurs at the binodal (B) resulting in the completely reversible Type IV(b) isotherm illustrated in Figure 7c.

The temperature is not the only aspect affecting hysteresis. For a given adsorptive at a given temperature, the pore width determines if hysteresis occurs. This is illustrated in Figure 8 which shows a schematic, simplified illustration of the shifted phase diagram for slit-like mesopores with two different widths together with the resulting isotherm Types IV(a) and IV(b). The critical point of confined fluid shifts to lower pressures and lower temperatures compared to the bulk fluid.<sup>[69,77,78]</sup> Additionally, the triple point shifts to lower temperatures,<sup>[69,71,77–80]</sup> which could be also observed in experiments with mesoporous silica.<sup>[71,72,81]</sup> However, details of the sorption and phase behavior below the triple point are not completely understood, yet.

As already mentioned, near the pore critical point, the hysteresis critical temperature can be defined. Hysteresis leading

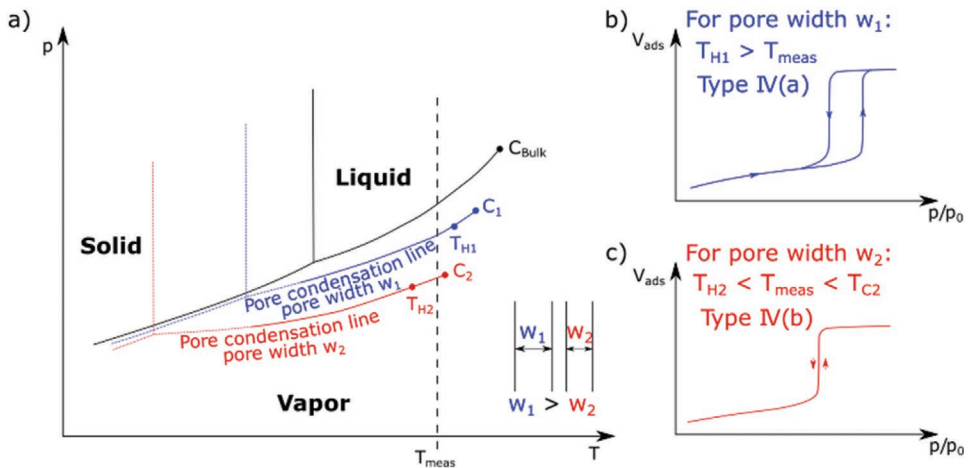


**Figure 8.** Schematic shift of the phase diagram for fluid confined in a slit pore with width  $w_1$  and  $w_2$  ( $w_1 > w_2$ ) and resulting isotherm types IV(a) and IV(b). a)  $T-p$  diagram for bulk fluid (black) and fluid confined in a pore with width  $w_1$  (blue) and width  $w_2$  (red), respectively. Pore condensation lines terminate in the pore critical points  $C_1$  and  $C_2$ . Near the pore critical point, the hysteresis critical temperature ( $T_{H1}, T_{H2}$ ) can be defined which is the temperature below which experimental hysteresis can be observed. Adapted with permission.<sup>[30]</sup> Copyright 2004, Kluwer Academic Publishers. In addition to the shift in the critical points, a shift of the triple point region to lower temperatures can be observed (e.g.,<sup>[71,72,81]</sup>). b) Materials with pore width  $w_1$  exhibit a Type IV(a) isotherm at the measurement temperature  $T_{meas}$  ( $T_{meas} < T_{H1}$ ). c) Materials with smaller pores of width  $w_2$  lead to a Type IV(b) isotherm ( $T_{H2} < T_{meas} < T_{C2}$ ).

to a Type IV(a) isotherm only occurs if the measurement temperature is below the hysteresis critical temperature. In the illustrated example, a Type IV(a) isotherm (Figure 8b) can be observed for the larger pores of size  $w_1$ . In contrast, a reversible Type IV(b) isotherm is observed for the smaller pores of size  $w_2$  due to the shifted hysteresis critical temperature. For argon and nitrogen adsorption at 87 and 77 K, respectively, pores smaller than  $\approx 4$  nm show a reversible adsorption behavior.

In addition to the delayed condensation during adsorption, more complex pore networks, for example, ink-bottle pores, show a shift in the liquid–vapor phase transition during desorption, for example, porous vycor glass or certain silica gels. Pore blocking or cavitation can cause delayed evaporation.<sup>[82]</sup> The pore neck width determines which of these mechanisms is present for a given adsorptive and temperature. For nitrogen and argon adsorption at 77 and 87 K, respectively, the critical neck width lies at 5–7 nm.<sup>[83–85]</sup> Cavitation occurs for pore necks smaller than the critical width. Both mechanisms affect the shape of hysteresis loops and must be taken into account for pore size and network analysis.

**Figure 9** illustrates both mechanisms with a schematic ink-bottle pore showing pore blocking (Figure 9a), an ink-bottle pore exhibiting cavitation (Figure 9b) and a corresponding pressure-density diagram of the pore cavity (Figure 9c).

In case of pore blocking (Figure 9a), the pore cavity remains filled until the neck evaporates at a lower relative pressure. In this case, the evaporation does not occur when crossing the binodal (Figure 9c) because no liquid–vapor interface is present for the pore cavity. The cavity evaporates when the neck evaporates, which occurs somewhere in the metastable region ( $B_{PoreBlocking}$ ) of the fluid confined in the pore cavity. In contrast, Figure 9b shows the desorption mechanism in case of cavitation. The neck size of the ink-bottle pores is now smaller than the critical neck width  $w_c$ . In this case, the liquid in the pore cavity evaporates while the neck remains filled. Looking at the

phase diagram for the pore cavity in Figure 9c neck and cavity remain filled during crossing the metastable region. Near the spinodal of the pore fluid ( $B_{Cavitation}$ ) a spontaneous nucleation of a bubble in the pore cavity followed by a liquid–vapor transition is induced, that is, cavitation induced desorption/evaporation represents a spinodal evaporation.<sup>[86]</sup>

As already mentioned, the origin of hysteresis and consequently, the shape of hysteresis loops have to be analyzed to obtain reliable information on the pore (network) structure of a material. **Figure 10** shows some selected types of hysteresis loops together with schematic illustrations of typical pore structures for the particular hysteresis shape.

Generally, materials show in the absence of pore blocking or cavitation induced evaporation a Type H1 hysteresis (Figure 10a). This is the case for mesoporous materials with independent cylindrical pores (e.g., MCM-41) or ordered 3D pore networks (e.g., MCM-48, KIT-6 silicas and some controlled pore glasses).<sup>[72,87]</sup> However, type H1 hysteresis was also observed for mesoporous 3DOM carbons, despite the occurrence of pore blocking.<sup>[88]</sup> Here, type H1 hysteresis was caused by the fact that for these highly ordered mesoporous carbon, consisting of ink-bottle pores, the distribution of pore necks is identical to the width of the cavity size distribution. However, pore blocking usually leads to type H2(a) or H2(b) hysteresis illustrated in Figure 10b,c, respectively. The steeper desorption branch compared to the adsorption branch in case of Type H2(a) hysteresis can be caused by a relatively wide size distribution of pore cavities compared to the neck size distribution. H2(a) hysteresis can also be caused by pore blocking induced percolation effects in pore networks which means that the liquid in the pore cavities evaporates when the largest neck evaporates.<sup>[38]</sup> Hence, the desorption mechanism is also depending on the connectivity to neighboring pores, not only on the neck size.<sup>[89]</sup> In contrast, type H2(b) hysteresis is typical for materials with a narrow pore cavity size distribution and in the absence of

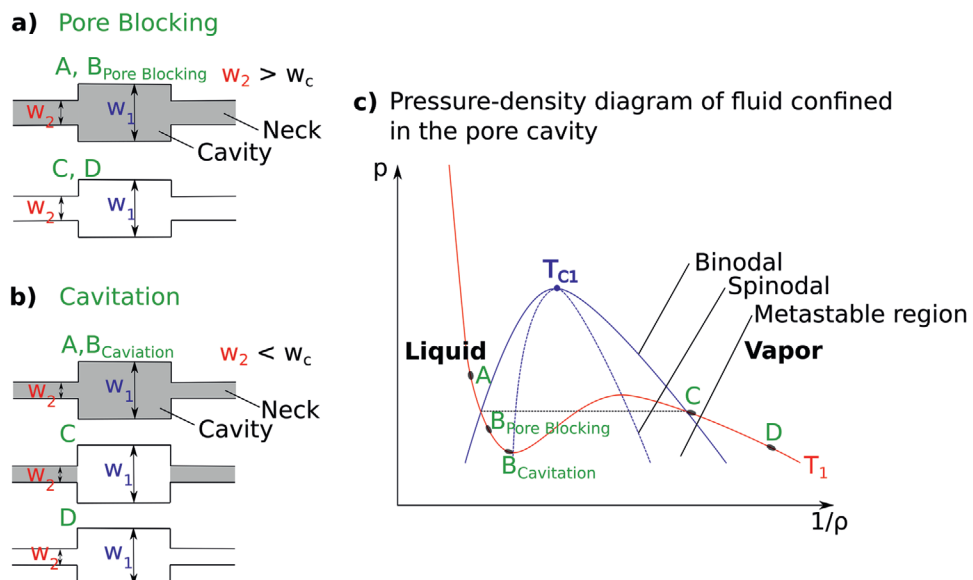


**Figure 9.** Schematic illustration of the desorption mechanism in case of pore blocking and cavitation, respectively. a) Illustration of an example ink-bottle pore during desorption in case of pore blocking. b) Illustration of an example ink-bottle pore during desorption in case of cavitation. c) Desorption mechanism and schematic pressure-density phase diagram of the pore (cavity) fluid with point B<sub>Pore Blocking</sub> in case of pore blocking and point B<sub>Cavitation</sub> in case of cavitation.

percolation effects.<sup>[38]</sup> In case of H2(b) hysteresis, the pore neck size distribution can be calculated from the desorption branch.

As already explained, cavitation occurs when the neck width is smaller than the critical neck width for a given adsorptive and temperature. This phenomenon usually leads to Type H2(a) hysteresis as shown in Figure 10d.

Type H5 loops (Figure 10e) are typical for materials containing both open and partially blocked mesopores. Due to the partially blocked pores, a cavitation induced steep step down can be observed in the desorption branch.

Hysteresis loops associated with pore condensation in mesopores only occur at relative pressures larger than  $\approx 0.35$  for nitrogen and argon at 77 K and 87 K, respectively. However, ZSM-5 materials with high Si/Al ratio (e.g., silicalite) for example show hysteresis in the relative pressure ranges from 0.1 to 0.25 and  $10^{-4}$  and  $10^{-2}$ , respectively, for nitrogen and argon adsorption.<sup>[90–92]</sup> This behavior cannot be associated with the pore filling/condensation in mesopores. It has been suggested that the hysteresis may indicate the occurrence of a phase transition of the zeolitic framework.<sup>[93]</sup> Hence, in such a case the application of standard methods for the assessment of surface area and pore size analysis may lead to meaningless BET surface areas and pore size distributions.<sup>[38,39]</sup>

### 5.3. Determination of Pore Size and Volume Distribution

Models describing the underlying adsorption mechanism are needed for the calculation of pore size distributions and pore volume. In case of Type I, Type IV, or combinations of Type I and IV isotherms, that is, materials containing only micro- and mesopores, the pore volume can be calculated using the Gurvich rule.<sup>[30]</sup> The nearly horizontal plateau near the bulk saturation pressure indicates that all pores are completely filled with liquid-like adsorbate. Assuming that the density of the

adsorbate equals the bulk liquid density, the pore volume can be calculated from the amount of gas adsorbed near the bulk saturation pressure, for example, at  $p/p_0 = 0.95$ . If a cylindrical pore geometry can be assumed, the average pore diameter of porous materials can be calculated by the following relation:

$$D_{4V/S} = \frac{4V_p}{(S_{\text{Total}} - S_{\text{ext}})} \quad (4)$$

The total surface area  $S_{\text{Total}}$  can be for instance calculated from the BET method (see Section 4).<sup>[10,30,60]</sup> The external surface area can be determined by applying for instance the comparison plot method in the region of relative pressure above the pore filling step (i.e., in case of mesopores above the pore condensation step). The comparison plot methods can also be utilized for assessing the pore volume of purely microporous materials<sup>[10,30,37]</sup> but their application is not any more straightforward for micro-mesoporous materials, particularly those containing narrow mesopores in the 2–4 nm range and efforts have been made to apply empirical corrections to the t-method.<sup>[94]</sup>

Within this context the application of advanced methods based on statistical mechanics, such as DFT based approaches is advantageous, because they take correctly into account the adsorption mechanism over the complete micro- and mesopore range. The details of the DFT method are discussed in the following sections.

The determination of pore volume by adsorption is more complicated if condensation in inter-particle voids can be observed during the adsorption process (e.g., Figure 5). In this case, the adsorbed amount increases at higher relative pressures and no plateau is observed. For this, gas adsorption needs to be coupled with methods such as mercury porosimetry.

Classical, macroscopic, and thermodynamic methods for mesopore size analysis, for example, the widely used BJH method, are based on the modified Kelvin equation. However, the validity of these methods becomes questionable especially for

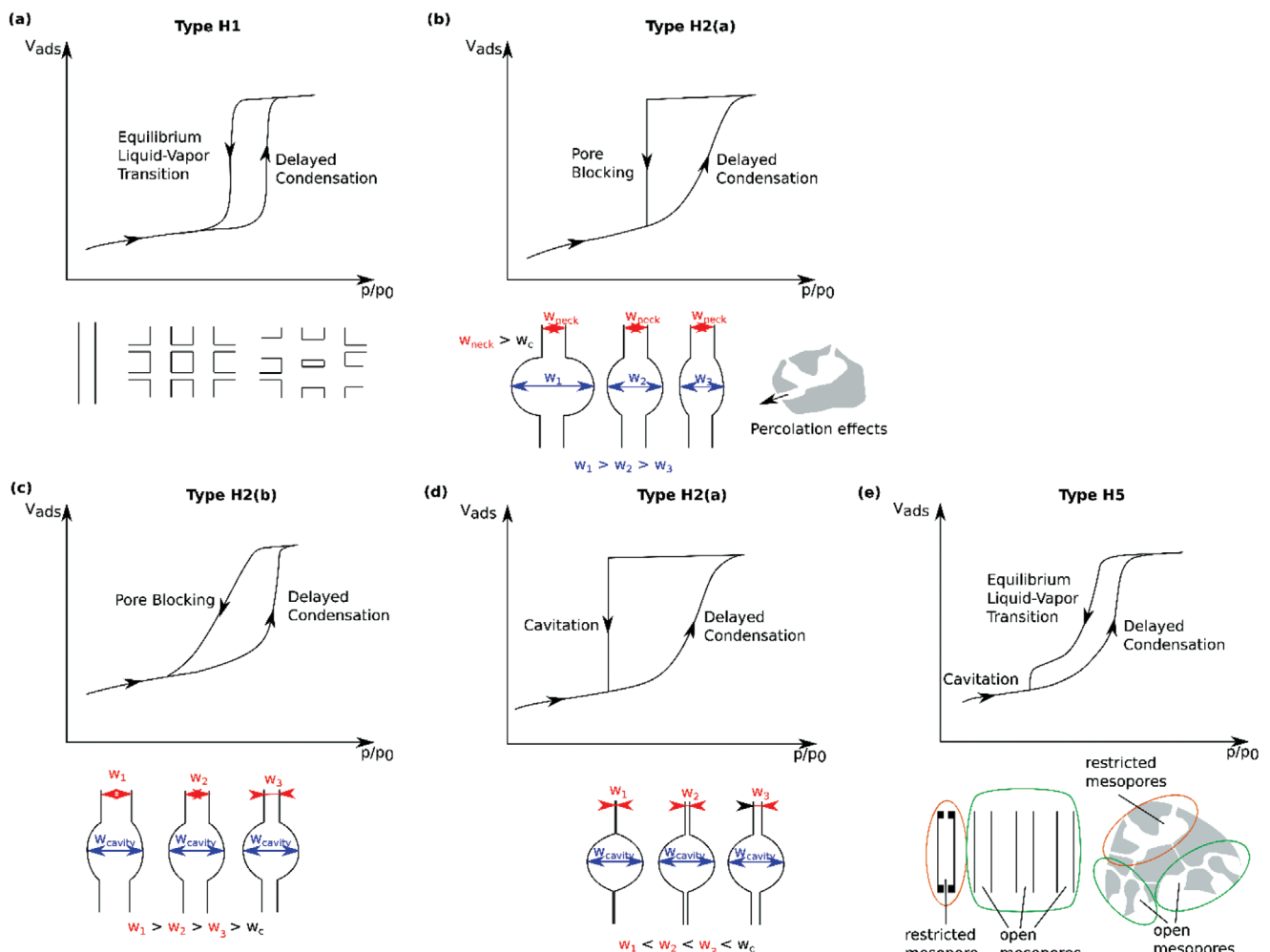


**Figure 10.** Adsorption hysteresis and their correlation with pore structure coupled with the underlying adsorption mechanism. a) Type H1 hysteresis. b) Type H2(a) hysteresis. c) Type H2(b) hysteresis. d) Type H2(a) hysteresis. e) Type H5 hysteresis. Adapted with permission.<sup>[32]</sup> Copyright 2014, Springer Nature.

small mesopores. In fact, these traditional macroscopic methods cannot accurately describe the confinement effect on the state of pore fluid.<sup>[31,45,95]</sup> This leads to large errors especially during pore size analysis of pores smaller than  $\approx 20$  nm. The BJH method and related macroscopic procedures may underestimate the pore size up to 20–30% for mesopores smaller than 10 nm.<sup>[30,31,45]</sup> This was clearly demonstrated with the aid of model mesoporous molecular sieves (e.g., M41S materials). Because of their high degree of order, the pore diameter of such model substances can be derived by independent methods (XRD, high resolution transmission electron microscopy, etc.).<sup>[31,45]</sup> A correction of these pore sizes is possible via calibration, however, calibrated methods are only valid for a small range of pore sizes.<sup>[96,97]</sup> The same situation can be observed in case of classical macroscopic methods for micropore analysis, for example, Dubinin–Radushkevich and the Horvath–Kawazoe methods.<sup>[33,98–100]</sup> These methods also often underestimate the pore size.

Applying microscopic methods based on molecular simulation (grand canonical Monte Carlo simulation) and DFT for pore size analysis can solve the above-mentioned problems

of macroscopic, thermodynamic methods. These advanced methods describe the structure of the adsorbed phase on a molecular level and capture all essential details of the underlying mechanism for micropore filling, pore condensation, and hysteresis.<sup>[33,45,101,102]</sup> Therefore, an accurate determination of the pore size distribution can be obtained in the complete micro- and mesopore range, which is most important for the textural characterization of hierarchically structured porous materials. Useful information can also be obtained from both the adsorption and desorption branches of the hysteresis loop, that is, it is possible to quantitatively predict the pore condensation and hysteresis behavior by taking into account the underlying adsorption–desorption mechanisms including the delay in condensation due to metastability of the pore fluid. Hence, contrary to the classical Kelvin equation based methods, the application of DFT based methods (e.g., NLDFT) calculate accurate pore size distributions also from the adsorption branch of the hysteresis loop. These advantages are crucial in the pore size analysis of materials, which give rise to H2, H3, H4, and H5 hysteresis loops.

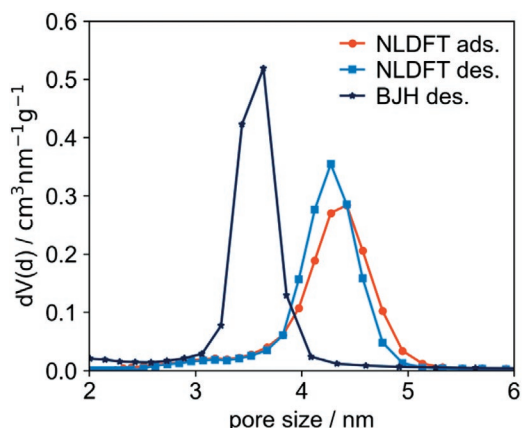


**Figure 11.** Comparison of mesopore size distribution of the mesoporous zeolite Y calculated with the BJH method and NLDFT using the adsorption and desorption branch of the Ar (87 K) isotherm by applying a dedicated metastable NLDFT adsorption branch kernel and an equilibrium NLDFT desorption branch kernel, respectively.

Figure 11 illustrates the good agreement of the mesopore size distribution of mesoporous zeolite Y obtained by applying NLDFT to the adsorption branch by applying a dedicated metastable adsorption branch kernel and to the desorption branch using an equilibrium desorption branch kernel, respectively. Additionally, Figure 11 demonstrates the underestimation of the mesopore size distribution determined with classical macroscopic methods such as the BJH method.

The determination of pore size distributions from experimental physisorption isotherms is based on the application

of DFT kernels. These are based on theoretical isotherms for a given adsorptive/adsorbent pair which are obtained by integrating density profiles of fluid in model pores. For the model pores, a certain pore geometry (slit, cylindrical, or spherical) has to be specified, which should fit the actual pore geometry of the porous material. As a result, a set of theoretical isotherms (kernel) calculated for a set of different pore sizes for a given adsorptive can be determined. The pore size distribution is then calculated using the integral adsorption equation, which correlates the kernel of theoretical isotherms with the experimental isotherm.<sup>[76,103,104]</sup> Figure 12 illustrates the principle of pore size analysis using DFT.

DFT based methods, in particular NLDFT, are now considered standard methods for pore size analysis of nanoporous materials.<sup>[45]</sup> This allows for the characterization of many adsorption systems also due to the availability of commercial software for various adsorbent systems and pore geometries (cylindrical, slit, spherical, or hybrids). However, as already discussed, it is crucial to assure that the chosen DFT and molecular simulation based methods are compatible with the experimental nanoporous systems.

An example for reliable pore size analysis in the complete micro- and mesopore range using NLDFT is shown in Figure 13 for the mesostructured zeolite Y using argon (87 K) adsorption.<sup>[105]</sup> The cumulative pore volume distribution curve allows directly for the determination of the micro- and mesopore volume.

The NLDFT pore size distribution obtained from the argon (87 K) isotherm data reveal for mesoporous Y-zeolite expected bimodal pore size distribution (see Figure 13), with micro- and mesopore peaks centered around 1.2 and 4.3 nm. The pore size

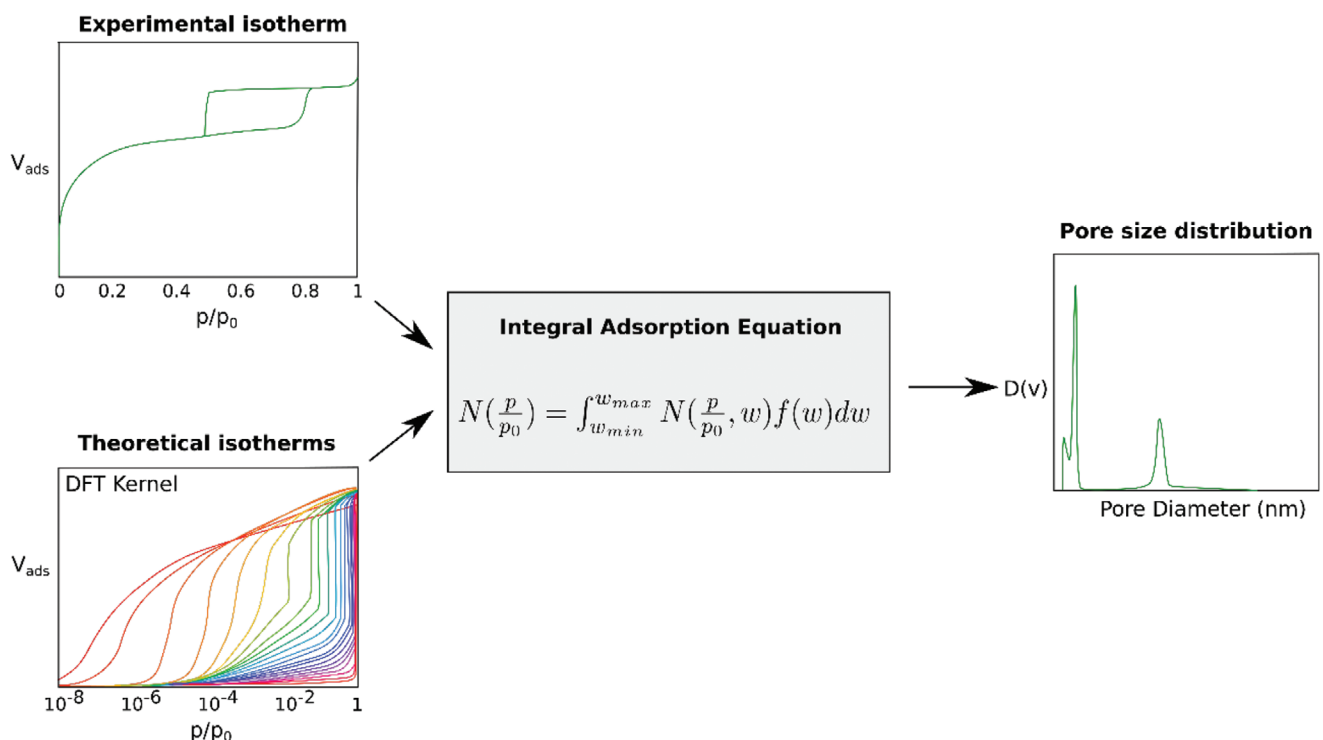


**Figure 12.** Calculation of DFT pore size distribution curves from experimental adsorption isotherms. Based on ref. [75].

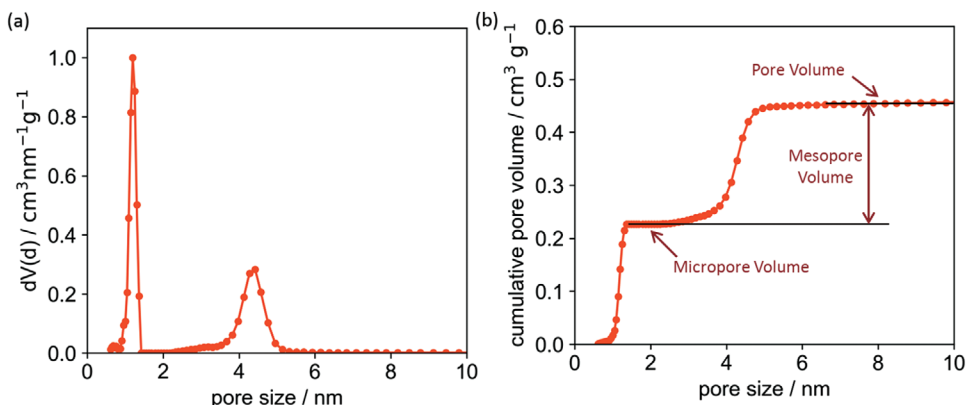


**Figure 13.** Pore size distribution of hierarchically structured mesoporous zeolite Y obtained by argon (87 K) adsorption and NLDFT analysis using a hybrid model assuming spherical micropores and cylindrical mesopores. a) differential pore size distribution (b) cumulative pore volume distribution.

distribution is calculated using a hybrid model consisting of spherical micropores and cylindrical mesopores. Assuming a proper pore geometry is essential for reliable pore size analysis using DFT. The pore geometry effect on the adsorption potential and the corresponding isotherm is schematically illustrated in **Figure 14** which shows characteristic adsorption potentials and isotherms dependent on the pore geometry for a micropore of size  $w$ .

Assuming a certain pore width, the relative pressure at which micropore filling occurs is increased from spherical to cylindrical to slit pores. This behavior is caused by the difference in adsorption potential, which is increased from slit to spherical pore geometry.

The effect of assuming an incorrect pore model for pore size analysis is illustrated in **Figure 15**. As already explained, the mesostructured zeolite Y exhibits a bimodal pore size distribution which can be reliably determined by applying dedicated NLDFT hybrid methods assuming a spherical pore model for the micropores and a cylindrical pore model for the mesopores. However, assuming a cylindrical pore model for the micropore range will cause underestimation of the micropore size distribution.

As already mentioned, an advantage of DFT based methods is the possibility of obtaining reliable pore size distributions from both the adsorption and desorption branch as they can describe not only the equilibrium but also the delay in condensation due to metastable adsorption films in mesopores. Using a metastable adsorption branch kernel now allows one to

accurately determine the pore size distribution from the adsorption branch, which is essential for materials exhibiting pore blocking or cavitation. This is shown in **Figure 16** for a hierarchically structured ZSM-5 zeolite and a disordered alumina catalyst.

The Ar (87 K) isotherm shown in Figure 16a shows a step down in the desorption branch which can be associated with cavitation induced evaporation of condensed liquid of larger mesopores. In this case, it is only possible to determine a reliable pore size distribution from the adsorption branch using a metastable adsorption branch kernel. The delayed evaporation due to cavitation leads to an artificial peak in the pore size distribution calculated from the desorption branch (Figure 16b).<sup>[38]</sup> The same behavior is also demonstrated for a disordered alumina catalyst in Figure 16c.

A drawback of the standard NLDFT methods is that they do not take sufficiently into account the chemical and geometrical heterogeneity of the pore walls, that is, usually a structureless (i.e., chemically and geometrically smooth) pore wall model is assumed. This mismatch between the theoretical assumption of a smooth and homogeneous surface and the experimental situation of an extremely heterogeneous surface may lead to artifacts in the PSD, which, however, are only clearly visible for disordered carbons if NLDFT is used for pore size analysis.<sup>[107,108]</sup> Much more realistic pore size analysis of carbons is possible by using quenched solid DFT, which takes into account the heterogeneity of carbon surfaces.<sup>[109]</sup>

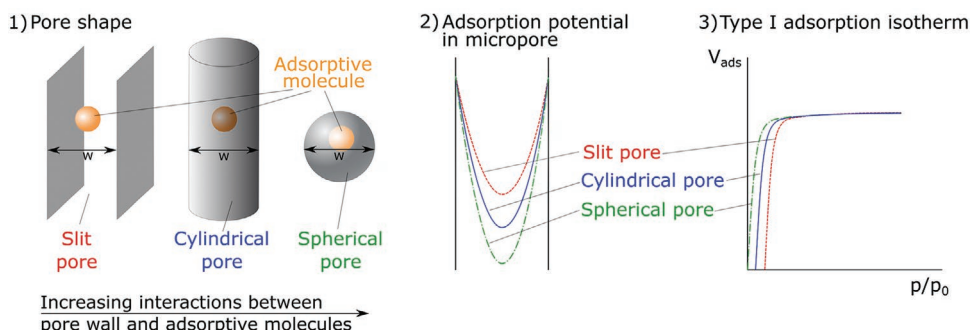


**Figure 14.** Schematic illustration of pore geometry effects on the adsorption potential of fluid confined in a micropore. 1) Schematic illustration of a slit, cylindrical, and spherical micropore. 2) Adsorption potential of a slit, cylindrical, and spherical micropore. 3) Resulting Type I adsorption isotherms

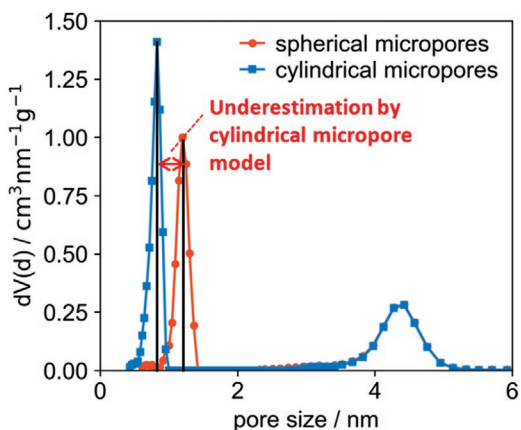


**Figure 15.** Pore size distribution of mesoporous zeolite Y determined by applying a dedicated NLDFT adsorption branch kernel on the adsorption branch of the Ar (87 K) isotherm using a cylindrical pore model and a hybrid model consisting of spherical micropores and cylindrical mesopores. As the pore structure of the hierarchical zeolite consists of cage-like spherical micropores and cylindrical mesopores, a reliable micropore size distribution can be determined using the hybrid model. The cylindrical pore model underestimates the size  $\approx 45\%$ .

#### 5.4. Assessing Aspects of Pore Network Characteristics

Physisorption allows one to analyze the pore network structure of micro- and mesoporous materials by comparing measurements with different adsorbents at various temperatures coupled with hysteresis scanning experiments. The following steps (a-d) can help to investigate the pore network structure and to verify the hierarchical structure of materials.<sup>[38,85,110,111]</sup> These steps a) and b) are also schematically illustrated in Figure 17.

a) First, comparison of the pore size distributions determined from the adsorption and the desorption branch using advanced DFT methods can help to detect restricted pores. The pore size distribution calculated from the adsorption (application of a proper metastable adsorption branch kernel) that takes into account the delayed (spinodal) condensation, see Section 5.2 and Figure 7) and desorption branch (application of equilibrium transition kernel) will coincide if the hysteresis can be entirely described by the occurrence of metastable pore fluid and the independent pore model can be applied. Hence this can be found for open, unrestricted pore networks and leads to type H1 hysteresis. For example, this is the case for ordered mesoporous molecular sieves such as MCM-41 and certain SBA-15 silicas which exhibit a 1D pore network structure.<sup>[30,31,38]</sup>

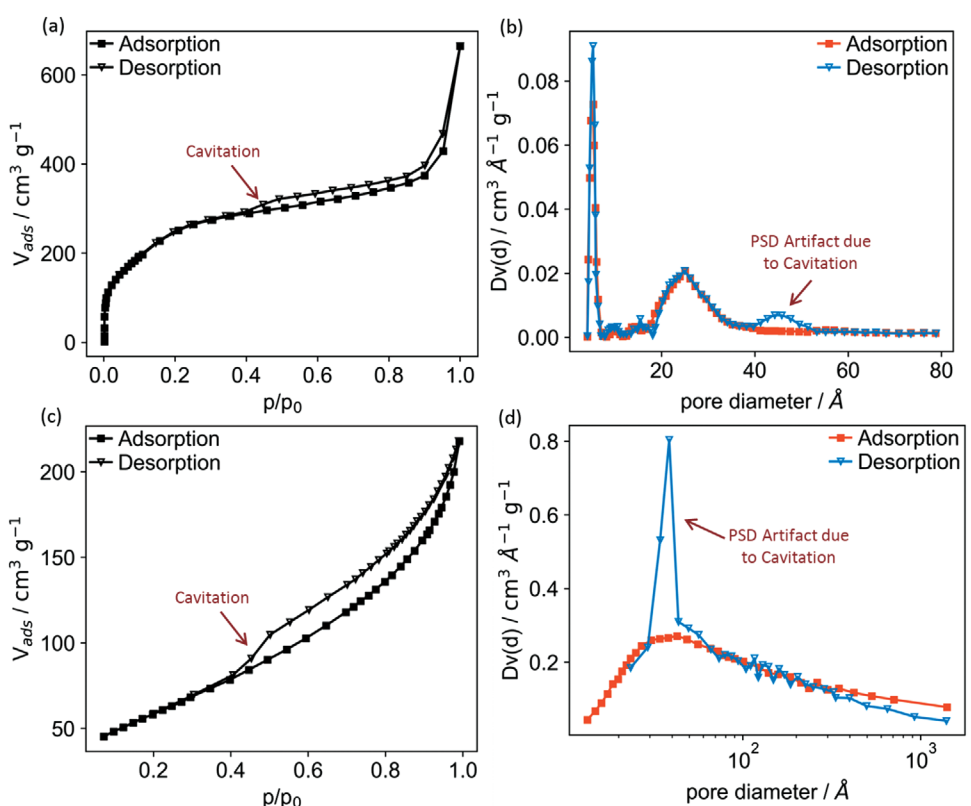


**Figure 16.** Pore size distribution artifacts due to cavitation. a) Ar (87 K) adsorption isotherm for hierarchically structured micro-mesoporous ZSM-5 zeolite and b) NLDFT pore size distribution of the micro-mesoporous ZSM-5 zeolite calculated from the adsorption and the desorption branch. The pore size distribution calculated with the desorption branch shows an artificial peak due to cavitation.<sup>[106]</sup> c) N<sub>2</sub> (77 K) adsorption on a disordered alumina catalyst. d) Pore size distribution of the alumina catalyst calculated from the adsorption and desorption branch Based on ref. [31].

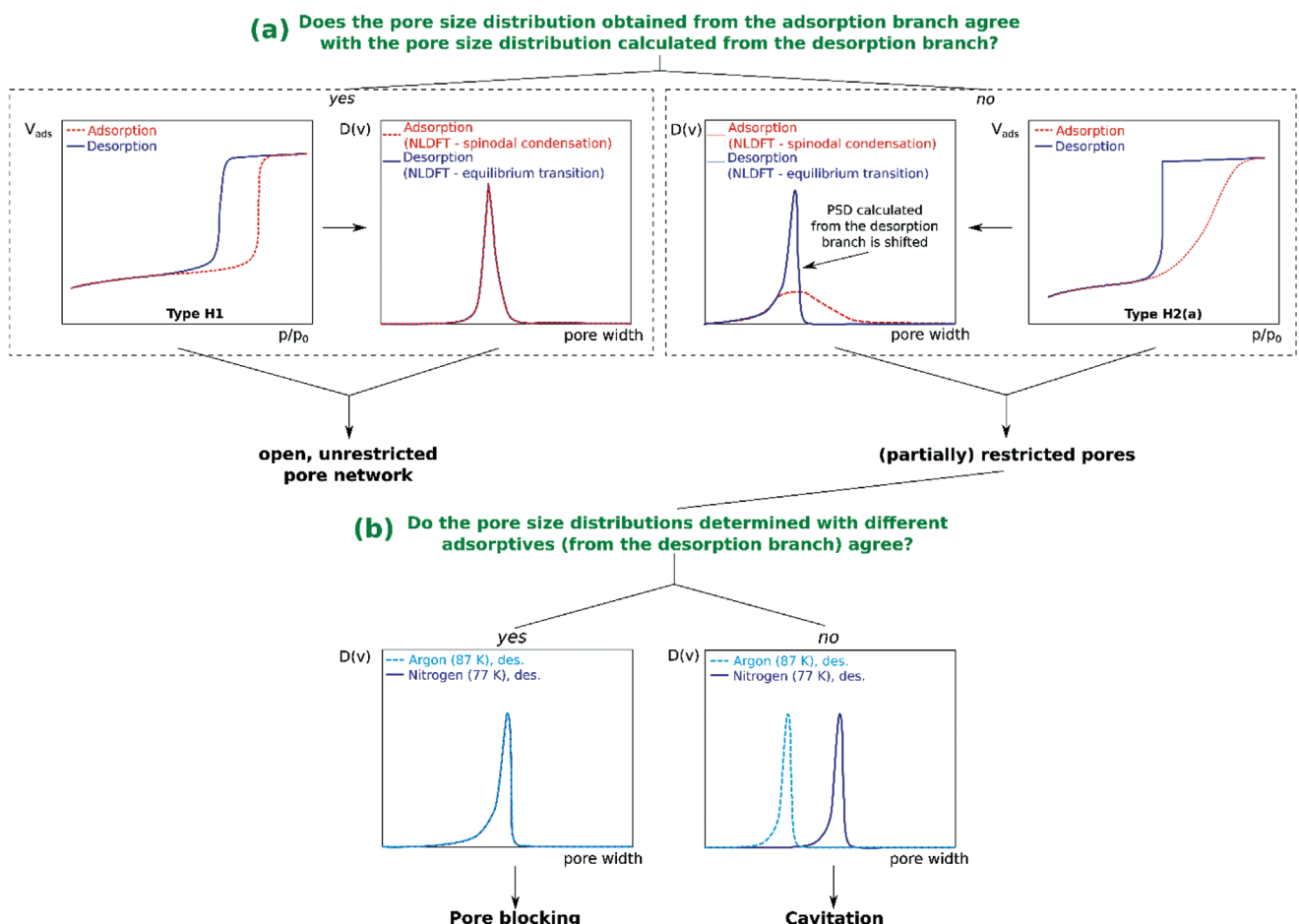


**Figure 17.** Advanced pore network analysis approach. a) Comparison of pore size distributions determined from the adsorption and desorption branch by applying dedicated metastable adsorption branch kernels and equilibrium desorption branch kernels, respectively, to check if restricted pores are present. b) In case of restricted pores, the comparison of pore size distributions obtained with different adsorbents can be used for the investigation of the desorption mechanism. A disagreement between the pore size distributions calculated from, for example, N<sub>2</sub> and Ar desorption branches indicates cavitation.

On the contrary, cavitation or pore blocking will cause a delayed evaporation in case of restricted pores. Therefore, the pore size distribution obtained from the desorption branch shifts to lower values and may exhibit a different width as compared with the pore size distribution curve obtained from the adsorption branch. As shown in Figure 17, this scenario usually arises in case of type H2 hysteresis. Summarizing, the here discussed disagreement between the pore size distributions calculated from the adsorption and desorption branch indicates that hysteresis is not entirely due to the existence of a metastable adsorption branch. Restricted pores and hence, pore network effects cause a shift of the desorption branch and hence, the pore size distribution calculated from the adsorption branch is more realistic in this case.<sup>[31]</sup> For example, this was observed for porous vycor glass in ref. [31].

However, it should be noted that for some ordered 3D pore networks, as present in certain KIT-6 and SBA-15 silica materials, advanced condensation may be observed. In this case, the effective nucleation barrier associated with the nucleation of the liquid phase is reduced in an interconnected pore network. As a consequence, the hysteresis loop is smaller in width as compared to the pseudo-1D SBA-15 system.<sup>[112,113]</sup> In this case, the position of the pore condensation pressure cannot be

quantitatively predicted by an approach, which is based on a single pore model. Hence, the pore size distribution calculated from the adsorption branch is shifted to smaller pore sizes. On the other hand, in this case, the desorption branch reflects the thermodynamic equilibrium and the pore size can be determined in a straightforward way from the desorption branch. Hence, mesopore connectivity (in absence of pore constrictions) may well affect the condensation pressure (by reducing the range of metastability) but not the pressure where desorption and evaporation occurs.<sup>[42]</sup>

b) Usually, restricted pores are present in case of a desorption pore size distribution, which is compared to the adsorption pore size distribution appreciably shifted to lower pore sizes. In this case, one can distinguish between pore blocking and cavitation by determining the desorption pore size distribution with different adsorbents, for example, nitrogen and argon at 77 and 87 K, respectively, which are at different thermodynamic states in the pores. If pore blocking/evaporation is the dominant mechanism, the evaporation pressure is controlled by the size of the necks (or connecting pores). Hence, the pore size distribution will not change depending on the chosen adsorbent. This can be seen, for example for porous vycor glass,<sup>[85]</sup> because there is a clear correlation between the pore neck size

and the relative pressure where pore evaporation occurs. In contrast, in case of cavitation, evaporation equals a spinodal liquid–vapor phase transition, which is a property of the chosen adsorptive. In this case, the disagreement between the pore size distributions obtained from the desorption branch clearly indicates cavitation induced evaporation.<sup>[85]</sup> For example, this was observed for KLE Silica in ref. [85].

c) Measurements at different temperatures may help during pore network analysis, as this will change the thermodynamics of the confined pore phase. This allows one to visualize pores of a pore network, which are not contributing to hysteresis with Ar (87 K) and N<sub>2</sub> (77 K) experiments. For example, smaller mesopores will contribute to hysteresis at lower measurement temperatures, and hence information about pore connectivity can be obtained.

d) Furthermore, hysteresis scanning experiments can be used to distinguish between pore blocking and cavitation. During hysteresis scanning, changing the direction of the gas pressure variation during the adsorption/desorption process leads to the generation of partial adsorption/desorption curves in the relative pressure range where hysteresis occurs. For example, a desorption scan is started at a relative pressure where pores are only partially filled. A recently developed statistical theory describes hysteresis and hysteresis scanning curves in 1D pore structures with structural disorder.<sup>[114,115]</sup> A quantitative description of scanning curves has been suggested by percolation models and methods based on molecular simulation (e.g.,<sup>[110,111]</sup> and references therein).

**Figure 18** shows a schematic illustration of hysteresis types and their behavior during hysteresis scanning experiments due to their pore network structure.

As already discussed, type H1 hysteresis (Figure 18a) is typical for materials with independent pores and ordered 3D pore

networks. In this case, delayed pore condensation is the only effect causing hysteresis. Hence, in this case, partially filling the pore system (e.g. up to point A) has no effect on the desorption hysteresis scan, which resembles the shape/type of the initial hysteresis loop, i.e. the boundary curve which is correlated with a completely filled pore system. The desorption mechanism in more complex pore networks can be a combination of equilibrium phase transition, pore blocking/percolation, and cavitation. In case of pore blocking, the interactions between neighboring pores may be dominating the desorption mechanism. Figure 18b illustrates a H2(a) hysteresis in case of pore blocking. In this case, the evaporation, which occurs at point P reflects a percolation transition. In this case, the scanning desorption isotherms usually converge in point B which is the lower closing point of the hysteresis loop. In case of a partially filled pore system, for example, at point A, a small fraction of pores will still be filled and hence, these pores empty at the lower closing point of the hysteresis as these pores may still be blocked by smaller necks.<sup>[6]</sup>

In case of necks smaller than the critical neck width (e.g., 5–7 nm for N<sub>2</sub> at 77 K), evaporation occurs due to cavitation. This leads to the H2(a) hysteresis in Figure 18c. At point C, spinodal evaporation occurs due to the limit of metastability, which induces the steep step down in the desorption curve. Here the mechanism of pore evaporation is not effected by neighbouring pores leading to desorption hysteresis scans which resemble the hysteresis shape/type of the initial boundary curve.

**Figure 19** shows the combination of the above-mentioned procedures for pore network analysis of the mesostructured, hierarchically organized zeolite Y. The combination of these methods was used to verify the hierarchical structure of the material in ref. [44].

Figure 19a shows the already explained Ar (87 K) adsorption isotherm together with the N<sub>2</sub> (77 K) isotherm. For

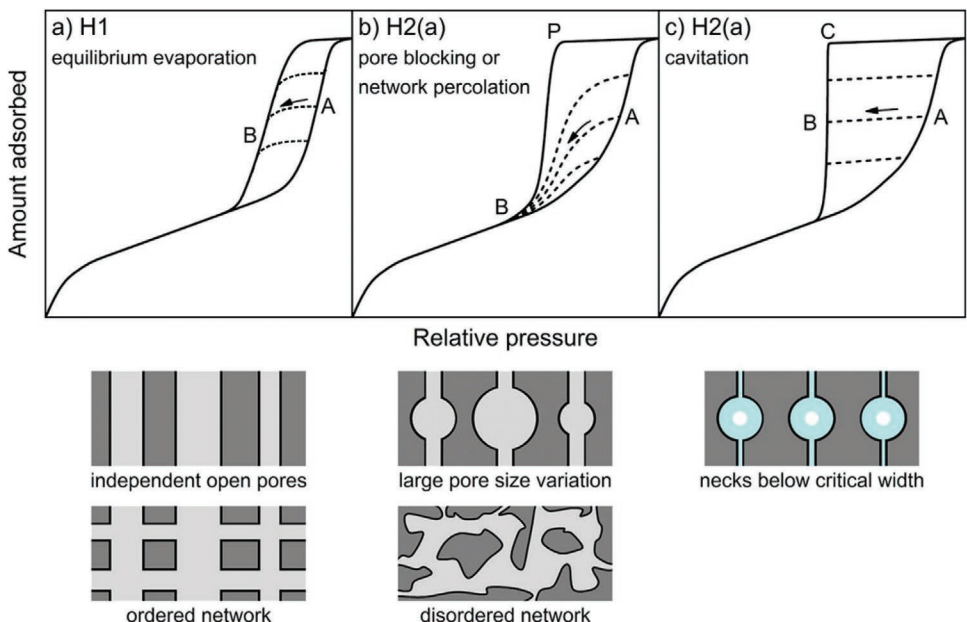


**Figure 18.** Schematic illustration of hysteresis types commonly observed in isotherms of mesoporous materials, along with corresponding scanning desorption isotherms. a) H1 hysteresis; highly ordered systems of unrestricted independent open pores and well-defined 3D pore networks. b) H2(a) hysteresis for pore blocking including percolation-induced pore evaporation; ink-bottle pores and disordered pore networks with wide PSDs and necks above a critical width. c) H2(a) hysteresis for cavitation-induced evaporation; ink-bottle pores and pore networks with necks below a critical width. Reproduced with permission.<sup>[6]</sup> Copyright 2020, American Chemical Society.

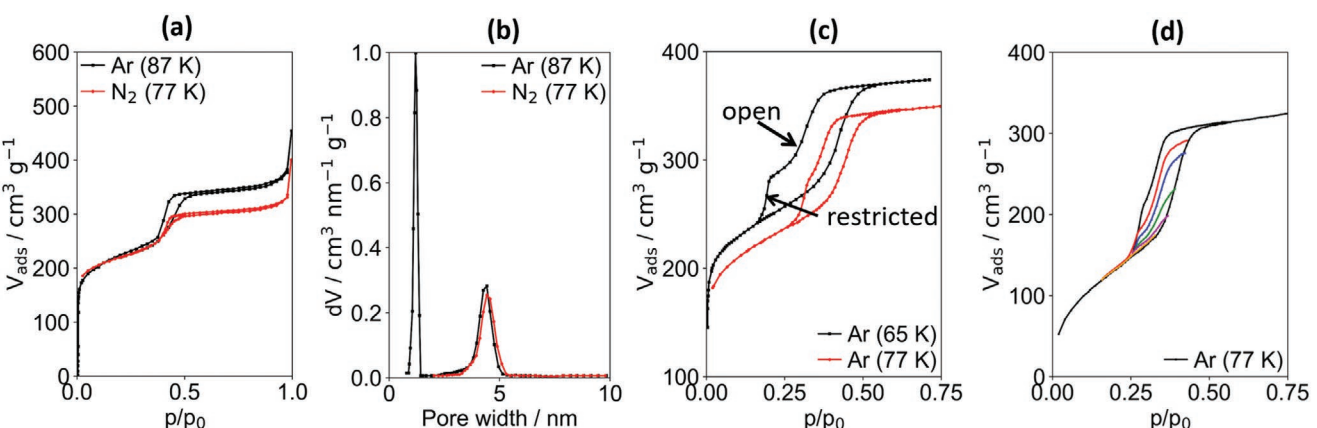


**Figure 19.** Argon and nitrogen adsorption on mesostructured zeolite Y. a) Ar (87 K) and N<sub>2</sub> (77 K) adsorption isotherms. b) NLDFT pore size distribution calculated from Ar and N<sub>2</sub> isotherms. c) Ar isotherms at 77 and 65 K. d) Hysteresis scanning isotherms with argon (77 K). Adapted with permission.<sup>[44]</sup> Copyright 2004, Wiley-VCH.

both adsorptives, a Type IV(a) isotherm with hysteresis was observed. The different widths of the hysteresis loops for argon and nitrogen indicate the different states of the mesopore fluid as nitrogen at 77 K is much closer to its hysteresis critical (and pore critical temperature).<sup>[31]</sup> The bimodal pore size distribution shown in Figure 19b was obtained by using NLDFT on the Ar (87 K) and N<sub>2</sub> (77 K) adsorption branch by applying a dedicated metastable adsorption branch kernel.

However, small mesopores do not contribute to hysteresis using argon and nitrogen at 87 and 77 K, respectively. Therefore, no information on the connectivity of these small mesopores can be obtained from the hysteresis loops. Hence, one has to change the thermodynamic state of the confined fluid to obtain information on the connectivity of these pores. Argon adsorption experiments were performed at 77 and 65 K. In this case, the measurement temperature is now below the hysteresis critical temperature for the narrow mesopores (<4 nm) and the fluid inside these pores now contributes to hysteresis. Type H5 hysteresis was found for argon adsorption at 65 and 77 K, respectively, as shown in Figure 19c. As already discussed, this hysteresis loop can be associated with a majority of mesopores freely accessible and not constricted. However, the access to a smaller amount of mesopores is constricted by smaller pore necks or some pores are only accessible through micropore channels of the zeolite. Hysteresis scanning experiments (Figure 19d) revealed that emptying of the restricted pores can be associated with cavitation. An advanced analysis of the described experiments allows one to differentiate between different types of interconnected pore networks and to quantify the accessible pore volume. In this case, 64% of the mesopores were freely accessible, while 36% were constricted by micropore channels.<sup>[44]</sup>

Summarizing, we have demonstrated here the application of a comprehensive toolbox of physisorption-based methodologies for advanced pore network analysis. While the nature of connectivity of the restricted mesopores follows directly from advanced gas adsorption studies, only limited information about the connectivity of the freely accessible mesopores can be achieved by physisorption analysis alone. To obtain additional information on the connectivity of the freely accessible mesopores advanced

gas adsorption experiments can be coupled with complementary techniques based on electron tomography.<sup>[44]</sup>

Hence, in order to obtain additional insights into the pore connectivity of hierarchical materials it is necessary to apply additional, complimentary experimental techniques as already indicated in the introduction,<sup>[3–7]</sup> for example, combining advanced physisorption with complimentary methods such as NMR-cryoporometry<sup>[116]</sup> and electron tomography.<sup>[1,3]</sup> In addition, the underlying adsorption and desorption mechanisms can be studied by coupling adsorption with techniques based on small angle scattering, that is, SANS and SAXS. In such in situ-SAXS or in situ-SANS experiments, neutron or X-ray scattering data are acquired during the adsorption and desorption steps of a physisorption experiment. The method is based on the contrast matching between the bulk material and the adsorptive.<sup>[5,6]</sup> It offers valuable information regarding the underlying mechanisms of the adsorption, phase behavior, and pore network structure including pore connectivity.

Very recently even hysteresis scanning experiments could be performed in in situ-SAXS-physisorption experiments, which revealed pore size gradients in disordered monolithic silica mesopore networks.<sup>[6]</sup>

## 6. Macropore Analysis

While gas adsorption can be utilized to assess the pore network characteristics of porous materials exhibiting micro- and mesopores, additional, complimentary techniques need to be utilized for assessing macropores. An overview of various techniques which can be utilized for macropore analysis, including liquid intrusion methods such as contact porosimetry, capillary flow porometry, and mercury porosimetry had been given by IUPAC in 2012.<sup>[40]</sup>

Among them, mercury porosimetry is still considered to be the state of the art method for textural analysis of macroporosity<sup>[40]</sup> and is widely accepted for pore size analysis of various materials including catalysts and their supports, building materials, and pharmaceutical tablets.

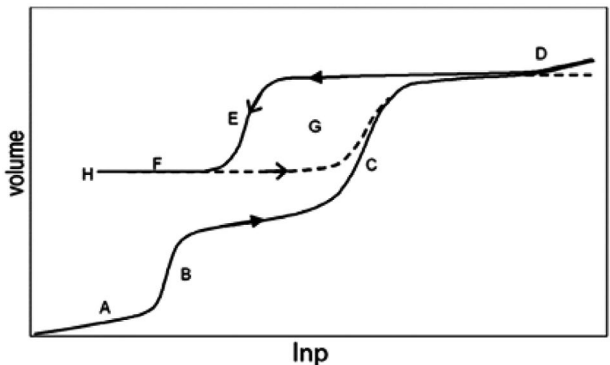


**Figure 20.** Schematic illustration of two consecutive mercury intrusion/extrusion cycles. Reproduced with permission.<sup>[40]</sup> Copyright 2011, De Gruyter.

The main attraction of this technique is that it allows pore size analysis to be undertaken over a wide range of mesopore–macropore widths (from  $\approx 4$  nm up to  $>400$   $\mu\text{m}$ ) in a fast and highly reproducible way.<sup>[117]</sup> In contrast to physical adsorption of fluids such as nitrogen and argon at their boiling temperatures, where the adsorbed phase completely wets the pore walls, liquid metals such as mercury do not wet the majority of materials at or close to room temperature. Hence, (hydraulic) pressure  $p_h$  must be applied to force liquid metals into pores. In case of cylindrical pores, the Washburn equation shows the relation between pore radius  $r$  with the hydraulic pressure  $p_h$ , which can be used for the calculation of pore size distributions:

$$p_h \cdot r = -2\gamma \cos\theta \quad (5)$$

The surface tension of mercury,  $\gamma$ , depends on the sample material and on temperature. At room temperature, a typical value is  $480$  mN  $\text{m}^{-1}$ . The contact angle  $\theta$  depends on the nature of the solid surface and lies typically between  $125^\circ$  and  $150^\circ$ . The contact angles of mercury with various solids can be found, for instance, in refs.<sup>[30,40,118]</sup>, but can also be determined experimentally.<sup>[30]</sup> If the value is unknown,  $\theta = 140^\circ$  may be used.

Figure 20 shows two typical intrusion/extrusion cycles for the intrusion and extrusion of mercury as a function of pressure (i.e.,  $\ln(p)$ ).

Part (A) corresponds to a compression of the powder, which is followed by intrusion into interparticle voids in region (B). In part (C), the pores are filled with mercury. At higher pressures, compression is possible for some materials in range (D). Due to hysteresis (H), extrusion occurs at a smaller pressure than intrusion (E). Usually, some mercury is entrapped by the sample in the first cycle which prevents the loop from closing leading to part (F).<sup>[40]</sup> This phenomenon was investigated by molecular simulation studies<sup>[41,43,119,120]</sup> and experiments in materials exhibiting well defined pore systems.<sup>[121]</sup> These studies revealed that entrapment is solely associated with kinetic effects during mercury extrusion mainly coupled with the tortuosity of a disordered pore network; this may lead to the rupture of mercury bridges in pore constrictions during extrusion.<sup>[43]</sup> Normally, the loop closes in following cycles, which means that there is no further entrapment of mercury.

However, the following cycles continue to show hysteresis (G), which is caused by nucleation barriers due to the formation of a vapor–liquid interface during the extrusion, while the intrusion branch reflects in the absence of pore blocking/percolation effects the equilibrium liquid–vapor transition. The latter also follows from systematic experiments on porous glasses materials coupled with approaches based on statistical mechanics such as DFT and molecular simulation.<sup>[41–43,119]</sup> This microscopic approach based on statistical mechanics has provided a molecular theory of mercury porosimetry and also a unified framework for understanding both gas adsorption and mercury porosimetry. Hence, the mechanisms of mercury intrusion/extrusion corresponds to pore evaporation/desorption and pore condensation/adsorption, respectively, in gas adsorption. Pore network effects such as pore blocking and related percolation phenomena will affect the intrusion branch.

Mercury porosimetry has been demonstrated to be a key method for assessing the combined meso–macropore structure of hierarchically structured materials. An example is shown in Figure 21 which shows a series of mercury intrusion/extrusion cycles into a hierarchically structured silica monolith (Figure 21 left) with well-defined macro-and mesoporosity (Figure 21 right) resembling Type II hierarchy with regard to the classification suggested in ref. [122].

The intrusion/extrusion curves at lower pressures correspond to the filling/emptying of the macroporous through-pores, while the intrusion/extrusion curves at higher pressures correspond to the mesopore filling/emptying. The graph at the right of Figure 21 reveals the bimodal pore size distribution of this truly hierarchically structured meso/macroporous silica monolith, demonstrating how powerful mercury intrusion/extrusion porosimetry is with regard to assessing multimodal pore size distributions over a wide range of pore sizes.

Intrusion/extrusion hysteresis is observed for both pore systems, but remarkably no entrapment is associated with the intrusion/extrusion cycles into the mesopore network. It was possible to show in these systematic studies that for given experimental parameters (e.g., equilibration time etc.) the occurrence and amount of entrapment depends on the macro-(through) pore structure which controls the mass transfer to and from the mesopores. Hence, the lack of entrapment after extrusion from the monolith mesopore system serves as an indication that the rate of mass transfer in and out of the mesopores appears to be fast enough to avoid fragmentation of liquid during extrusion (which would lead to entrapment). In contrast one observes always entrapment in case of powders where the disordered interparticular porosity acts as the effective through-pore systems, independent from the uniformity of the intraparticle pore network.<sup>[123]</sup>

Hence, the absence of entrapment for the silica monolith (as shown in Figure 21) could be correlated with the unique texture of these hierarchical pore networks consisting of a well-defined mesopore system surrounded by macroporous through-pores. However, this confirms that the extrusion is only possible through the nucleation of vapor, as already mentioned before. This occurs close to the liquid–vapor spinodal of the confined mercury and hence these data are in line with the extrusion branch and can be considered a metastable branch of

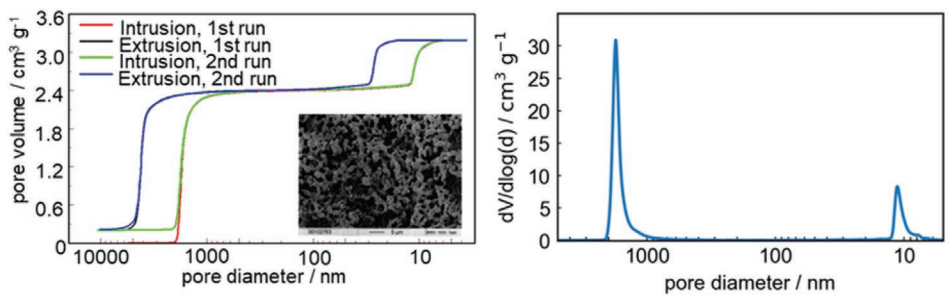


**Figure 21.** Consecutive intrusion/extrusion cycles of mercury obtained on a hierarchical silica monolith and corresponding pore size distribution of the material. Adapted with permission.<sup>[123]</sup> Copyright 2008, Elsevier.

the hysteresis loop similar to the adsorption branch of capillary condensation hysteresis for wetting fluids.

Further insights concerning the sorption and phase behavior of mercury could be obtained very recently by systematic intrusion/extrusion experiments in KIT-6 silica (an ordered mesoporous molecular sieve exhibiting an ordered 3D pore network). Contrary to other well-known ordered mesoporous silica such as MCM-41 and certain SBA-15 silica materials, where the mercury intrusion/extrusion behavior can be appreciably affected by their mechanical stability,<sup>[124–126]</sup> KIT-6 silica is capable of withstanding the extremely high pressures in a mercury porosimetry experiment. Hence, it was possible to utilize KIT-6 mesoporous molecular sieves for quantitatively testing the validity of the Washburn equation applied to mercury intrusion for pore size analysis.<sup>[42]</sup> These studies on KIT-6 silicas also allowed investigating the analogies between condensation/evaporation mechanisms of wetting ( $N_2$  at 77 K) and non-wetting (Hg at 298 K) fluids as a function of the pore size confirming the thermodynamic consistency between extrusion and capillary evaporation/condensation.<sup>[42]</sup> This is

demonstrated in **Figure 22** which shows the  $N_2$  isotherm at 77 K on one of the KIT-6 in comparison with the calculated corresponding mercury adsorption/desorption isotherm (obtained from the hydraulic pressure needed to push mercury into the pores is correlated with the corresponding effective vapor pressure). While capillary condensation of  $N_2$  occurs at pressures smaller than the saturation pressures, the vapor–liquid phase transition for the non-wetting fluid mercury occurs at pressures, which are larger than the saturation pressure of bulk mercury at the experimental temperature, leading to a striking reversed symmetry observed between the two sets of curves.

The effect of pore size on both the vapor–liquid phase transition of the wetting adsorptive ( $N_2$ , 77 K) and the non-wetting fluid (Hg) could also be investigated, and the results are summarized in the schematic phase diagram in **Figure 22b**. These experiments on the highly ordered mesoporous molecular sieves KIT-6 confirm the analogy between mercury intrusion/extrusion and gas adsorption (pore condensation/evaporation).

Summarizing, mercury porosimetry is a key technique for the textural characterization of hierarchically organized zeolites.

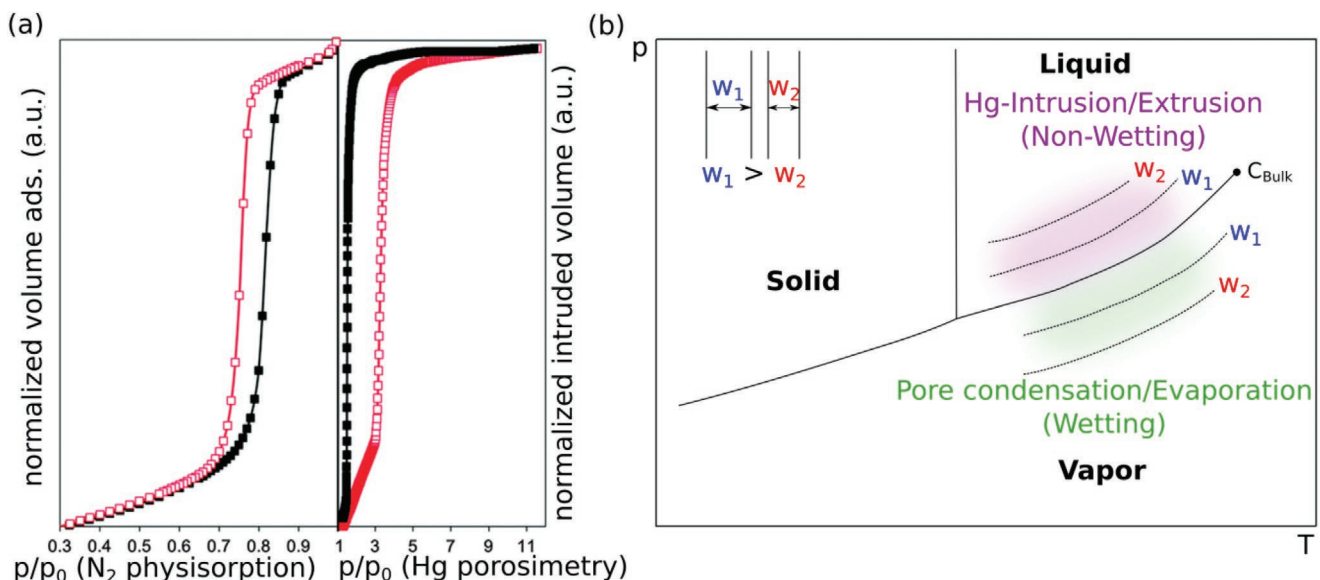


**Figure 22.** Equivalence of mercury porosimetry and gas sorption: Phase behavior of wetting and non-wetting fluids in mesopores. a) Adsorption and desorption isotherms for KIT-6 silica of wetting ( $N_2$ , 77 K) and the corresponding equivalent gas sorption isotherms of a non-wetting fluid (Hg, 298 K) converted from the mercury porosimetry data. b) Schematic phase diagram of bulk and confined fluid showing the symmetry between pore condensation/evaporation and Hg-intrusion/extrusion. Adapted with permission.<sup>[42]</sup> Copyright 2016, The Royal Society of Chemistry.

The mechanism of intrusion and extrusion are the same as for condensation/adsorption and evaporation/desorption in gas adsorption. Within this context, the position of the intrusion branch is governed by the size of pore entrances in case of the presence of pore restrictions. It is strongly recommended not only to measure one intrusion curve alone, but instead at a minimum also the extrusion curve. It is now possible to identify certain characteristic features of the observed hysteresis and associate these with pore network characteristics. Furthermore, reproducibility of the hysteresis loop in a second intrusion/extrusion cycle indicates that the pore structure of the samples was not irreversibly affected in the first cycle. The progress made in understanding the mechanisms which govern intrusion/extrusion hysteresis and entrapment not only significantly improves the interpretation of mercury porosimetry data but also allows one to apply and develop advanced experimental protocols (including multiple intrusion/extrusion cycles) leading to an enhanced and more reliable structural characterization of a macro-mesopore networks.

## 7. Summary and Conclusions

This tutorial deals with the characterization of nanoporous materials with focus on hierarchically ordered materials, such as hierarchical zeolites, which exhibit pores potentially spanning the whole range from micro- to macropores. Hierarchically ordered zeolites offer improved applicative properties (e.g., activity, selectivity, and conversion), but the structure-property-performance relationships are not sufficiently well understood. Hence, an advanced targeted textural characterization coupled with transport properties is needed. Within this context, we discuss in this tutorial selected aspects of textural characterization, that is, we focus mainly on the application of advanced physisorption methodologies for micro- and mesopore analysis but also address the assessment of the macropore structure by mercury porosimetry.

In fact, during recent years major progress has been achieved in the understanding of the adsorption, pore condensation, and hysteresis behavior of fluids in nanoporous materials. This has led to significant progress in the structural characterization by physical adsorption, also because of the development and availability of theoretical procedures based on statistical mechanics, for example, NLDFT and molecular simulation coupled with advanced experimental protocols for the adsorption of various subcritical fluids (e.g., argon adsorption at 87 K). It has been demonstrated that the application of DFT and molecular simulation based methods on high-resolution experimental adsorption isotherms provides a much more accurate and comprehensive pore size analysis over the complete range of micro-and mesopores as compared to classical, macroscopic methods (e.g., Kelvin equation-based approaches such as the BJH method). The key results of these advances and corresponding recommendations for a reliable application of gas adsorption techniques for material characterization have been summarized in a widely accepted report of IUPAC.<sup>[39]</sup>

The adsorption behavior in hierarchical pore structures is governed by a combination of various phenomena including micropore filling, pore condensation, pore blocking/percolation, and cavitation induced evaporation, which is reflected in the shape of the adsorption isotherm and characteristic types

of adsorption hysteresis. Hence, a proper interpretation of pore condensation and hysteresis loops coupled with advanced experimental protocols (including hysteresis-scanning experiments) allows one to obtain detailed information about pore network characteristics. Within this context, it will be useful to develop more advanced data reduction methods, which are based on more realistic models for describing the complex pore structure of hierarchical porous materials.

Nevertheless, a comprehensive toolbox of physisorption-based methodologies for advanced pore network analysis is now available. Combined with the advances made in understanding the mechanisms which govern mercury intrusion/extrusion hysteresis, we are now in a position to arrive at a quite detailed and comprehensive assessment of the pore network characteristics of hierarchical organized zeolites. However, while the nature of connectivity of the restricted mesopores follows directly from advanced gas adsorption studies, only limited information about the connectivity of the freely accessible mesopores can be achieved by physisorption analysis alone. Hence, it needs to be clearly stated that, although not discussed in this tutorial, it is necessary to apply complimentary experimental techniques (e.g., positron annihilation lifetime spectroscopy-PALS, NMR-cryoporometry, and electron tomography) and combinations of advanced physisorption with advanced scattering methods (e.g., in situ-SANS or in situ- SAXS) for obtaining a complete pore network characterization of hierarchically structured materials. To fully elucidate the details of an interconnected, disordered hierarchical pore network and to fully correlate pore network characteristics with transport properties and application performance, more efforts are still needed; in fact, it will be necessary to combine and integrate such complementary experimental techniques coupled with the development of enhanced experimental protocols and advanced methods for data interpretation.

## Acknowledgements

The work was supported by the Deutsche Forschungsgemeinschaft (DFG, German Research Foundation)—Project-ID 416229255 - SFB 1411.

Open access funding enabled and organized by Projekt DEAL.

## Conflict of Interest

The authors declare no conflict of interest.

## Keywords

hierarchically ordered porous materials, hysteresis, mercury porosimetry, nanopores, physical adsorption, pore size analysis, surface area

Received: December 14, 2020

Revised: January 15, 2021

Published online: February 9, 2021

- [1] T. Müllner, K. K. Unger, U. Tallarek, *New J. Chem.* **2016**, *40*, 3993.
- [2] D. Schneider, D. Mehlhorn, P. Zeigermann, J. Käger, R. Valiullin, *Chem. Soc. Rev.* **2016**, *45*, 3439.
- [3] A. Svidrytski, A. Rathi, D. Hluskou, D. M. Ford, P. A. Monson, U. Tallarek, *Langmuir* **2018**, *34*, 9936.

- [4] J. Kärger, *Microporous Mesoporous Mater.* **2014**, *189*, 126.
- [5] O. Sel, A. Brandt, D. Wallacher, M. Thommes, B. Smarsly, *Langmuir* **2007**, *23*, 4724.
- [6] S. A. Kube, K. Turke, R. Ellinghaus, D. Wallacher, M. Thommes, B. M. Smarsly, *Langmuir* **2020**, *36*, 11996.
- [7] S. Mitchell, L. Gerchow, R. Warrington, P. Crivelli, J. Pérez-Ramírez, *Small Methods* **2018**, *2*, 1800268.
- [8] J. Rouquerol, D. Avnir, C. W. Fairbridge, D. H. Everett, J. M. Haynes, N. Pernicone, J. D. F. Ramsay, K. S. W. Sing, K. K. Unger, *Pure Appl. Chem.* **1994**, *66*, 1739.
- [9] P. Klobes, K. Meyer, R. G. Munro, *Porosity and Specific Surface Area Measurements for Solid Materials*, NIST, Gaithersburg, MD **2006**, p.960.
- [10] S. J. Gregg, K. S. W. Sing, *Adsorption, Surface Area, and Porosity*, Academic Press, London, NY **1982**.
- [11] J. Čejka, H. van Bekkum, A. Corma, F. Schueth, *Introduction to Zeolite Molecular Sieves*, Elsevier, Amsterdam **2007**.
- [12] G. Q. Lu, X. S. Zhao, in *Nanoporous Materials: Science and Engineering*, Imperial College Press, London **2004**, pp. 1–13.
- [13] W. Schwieger, A. G. Machoke, B. Reiprich, T. Weissenberger, T. Selvam, M. Hartmann, in *Zeolites in Catalysis: Properties and Applications* (Eds: J. Čejka, R. E. Morris, P. Nachtigall), The Royal Society of Chemistry, London **2017**, pp. 103–145.
- [14] J. García-Martínez, K. Li, G. Krishnaiah, *Chem. Commun.* **2012**, *48*, 11841.
- [15] P. G. Blakeman, E. M. Burkholder, H.-Y. Chen, J. E. Collier, J. M. Fedeyko, H. Jobson, R. R. Rajaram, *Catal. Today* **2014**, *231*, 56.
- [16] N.-L. Michels, S. Mitchell, J. Pérez-Ramírez, *ACS Catal.* **2014**, *4*, 2409.
- [17] E. T. C. Vogt, B. M. Weckhuysen, *Chem. Soc. Rev.* **2015**, *44*, 7342.
- [18] V. P. S. Caldeira, A. Peral, M. Linares, A. S. Araujo, R. A. Garcia-Muñoz, D. P. Serrano, *Appl. Catal., A* **2017**, *531*, 187.
- [19] S. Ren, B. Meng, X. Sui, H. Duan, X. Gao, H. Zhang, P. Zeng, Q. Guo, B. Shen, *Ind. Eng. Chem. Res.* **2019**, *58*, 7886.
- [20] D. Kerstens, B. Smeyers, J. V. Waeyenberg, Q. Zhang, J. Yu, B. F. Sels, *Adv. Mater.* **2020**, *32*, 2004690.
- [21] S. M. Al-Jubouri, N. A. Curry, S. M. Holmes, *J. Hazard. Mater.* **2016**, *320*, 241.
- [22] J. Liu, X. Yang, C. Wang, L. Ye, H. Sun, *Adsorpt. Sci. Technol.* **2019**, *37*, 530.
- [23] B. Besser, H. A. Tajiri, G. Mikolajczyk, J. Mo, S. Odenbach, R. Glas, *ACS Appl. Mater. Interfaces* **2016**, *8*, 3277.
- [24] S. J. J. Titinchi, M. Piet, H. S. Abbo, O. Bolland, W. Schwieger, *Energy Procedia* **2014**, *63*, 8153.
- [25] W. Yu, L. Deng, P. Yuan, D. Liu, W. Yuan, F. Chen, *Chem. Eng. J.* **2015**, *270*, 450.
- [26] R. Li, S. Chong, N. Altaf, Y. Gao, B. Louis, Q. Wang, *Front. Chem.* **2019**, *7*, 505.
- [27] K. X. Lee, J. A. Valla, *React. Chem. Eng.* **2019**, *4*, 1357.
- [28] R. Skudas, B. A. Grimes, M. Thommes, K. K. Unger, *J. Chromatogr. A* **2009**, *1216*, 2625.
- [29] H.-J. Woo, L. Sarkisov, P. A. Monson, in *Studies in Surface Science and Catalysis*, Vol. 144, Elsevier, Amsterdam **2002**, p. 155.
- [30] S. Lowell, J. E. Shields, M. A. Thomas, M. Thommes, *Characterisation of Porous Solids and Powders: Surface Area, Pore Size and Density*, Kluwer Academic Publishers, Dordrecht, Netherlands **2004**.
- [31] M. Thommes, in *Nanoporous Materials: Science and Engineering* (Eds: G. Lu, X. Zhao), Imperial College Press, London **2004**, p. 317.
- [32] M. Thommes, K. A. Cychosz, *Adsorption* **2014**, *20*, 233.
- [33] P. A. Monson, *Microporous Mesoporous Mater.* **2012**, *160*, 47.
- [34] M. Thommes, *Chem. Ing. Tech.* **2010**, *82*, 1059.
- [35] K. Kaneko, T. Itoh, T. Fujimori, *Chem. Lett.* **2012**, *41*, 466.
- [36] M. Thommes, K. A. Cychosz, A. V. Neimark, in *Novel Carbon Adsorbents*, Elsevier, Amsterdam **2012**, p. 107.
- [37] F. Rouquerol, J. Rouquerol, P. Llewellyn, G. Maurin, *Adsorption by Powders and Porous Solids*, Academic Press, London **2013**.
- [38] K. A. Cychosz, R. Guillet-Nicolas, J. García-Martínez, M. Thommes, *Chem. Soc. Rev.* **2017**, *46*, 389.
- [39] M. Thommes, K. Kaneko, A. V. Neimark, J. P. Olivier, F. Rodriguez-Reinoso, J. Rouquerol, K. S. W. Sing, *Pure Appl. Chem.* **2015**, *87*, 1051.
- [40] J. Rouquerol, G. Baron, R. Denoyel, H. Giesche, J. Groen, P. Klobes, P. Levitz, A. V. Neimark, S. Rigby, R. Skudas, K. Sing, M. Thommes, K. Unger, *Pure Appl. Chem.* **2012**, *84*, 107.
- [41] F. Porcheron, P. A. Monson, M. Thommes, *Langmuir* **2004**, *20*, 6482.
- [42] R. Guillet-Nicolas, R. Ahmad, K. A. Cychosz, F. Kleitz, M. Thommes, *New J. Chem.* **2016**, *40*, 4351.
- [43] F. Porcheron, M. Thommes, R. Ahmad, P. A. Monson, *Langmuir* **2007**, *23*, 3372.
- [44] J. García-Martínez, C. Xiao, K. A. Cychosz, K. Li, W. Wan, X. Zou, M. Thommes, *ChemCatChem* **2014**, *6*, 3110.
- [45] J. Landers, G. Yu. Gor, A. V. Neimark, *Colloids Surf., A* **2013**, *437*, 3.
- [46] J. U. Keller, E. Robens, C. du Fresne von Hohenesche, in *Studies in Surface Science and Catalysis*, Vol. 144, Elsevier, Amsterdam **2002**, p. 387.
- [47] R. S. Mikhail, E. Robens, Wiley, Chichester **1983**.
- [48] K. Kaneko, T. Ohba, Y. Hattori, M. Sunaga, H. Tanaka, H. Kanoh, in *Studies in Surface Science and Catalysis*, Vol. 144, Elsevier, Amsterdam **2002**, p. 11.
- [49] ISO 9277:2010, Determination of the specific surface area of solids by gas adsorption—BET method, **2010**.
- [50] J. Silvestre-Albero, A. M. Silvestre-Albero, P. L. Llewellyn, F. Rodríguez-Reinoso, *J. Phys. Chem. C* **2013**, *117*, 16885.
- [51] S. C. Liang, *J. Phys. Chem.* **1953**, *57*, 910.
- [52] K. Poulter, M.-J. Rodgers, P. Nash, T. Thompson, M. Perkin, *Vacuum* **1983**, *33*, 311.
- [53] F. J. Sotomayor, K. A. Cychosz, M. Thommes, *Acc. Mater. Surf. Res.* **2018**, *18*, 34.
- [54] D. Lässig, J. Lincke, J. Moellmer, C. Reichenbach, A. Moeller, R. Gläser, G. Kalies, K. A. Cychosz, M. Thommes, R. Staudt, H. Krautscheid, *Angew. Chem., Int. Ed.* **2011**, *50*, 10344.
- [55] J. Silvestre-Albero, A. Silvestre-Albero, F. Rodríguez-Reinoso, M. Thommes, *Carbon* **2012**, *50*, 3128.
- [56] J. Garrido, A. Linares-Solano, J. M. Martin-Martinez, M. Molina-Sabio, F. Rodriguez-Reinoso, R. Torregrosa, *Langmuir* **1987**, *3*, 76.
- [57] D. Cazorla-Amorós, J. Alcañiz-Monge, A. Linares-Solano, *Langmuir* **1996**, *12*, 2820.
- [58] S. Dantas, K. C. Struckhoff, M. Thommes, A. V. Neimark, *Carbon* **2021**, *173*, 842.
- [59] J. García-Martínez, D. Cazorla-Amorós, A. Linares-Solano, in *Studies in Surface Science and Catalysis*, Vol. 128, Elsevier, Amsterdam **2000**, p. 485.
- [60] J. Rouquerol, F. Rouquerol, P. Llewellyn, G. Maurin, K. Sing, in *Adsorption by Powders and Porous Solids*, Academic Press, London **2013**, pp. 237–268.
- [61] S. Brunauer, P. H. Emmett, E. Teller, *J. Am. Chem. Soc.* **1938**, *60*, 309.
- [62] J. Rouquerol, P. Llewellyn, F. Rouquerol, in *Studies in Surface Science and Catalysis*, Vol. 160, Elsevier, Amsterdam **2007**, p. 49.
- [63] T. Keii, T. Takagi, S. Kanetaka, *Anal. Chem.* **1961**, *33*, 1965.
- [64] E. P. Barrett, L. G. Joyner, P. P. Halenda, *J. Am. Chem. Soc.* **1951**, *73*, 373.
- [65] J. C. P. Broekhoff, J. H. de Boer, *J. Catal.* **1967**, *9*, 8.
- [66] J. C. P. Broekhoff, J. H. De Boer, *J. Catal.* **1967**, *9*, 15.
- [67] J. C. P. Broekhoff, J. H. de Boer, *J. Catal.* **1968**, *10*, 377.
- [68] M. W. Cole, W. F. Saam, *Phys. Rev. Lett.* **1974**, *32*, 985.
- [69] M. Thommes, G. H. Findenegg, *Langmuir* **1994**, *10*, 4270.

- [70] A. V. Neimark, P. I. Ravikovitch, A. Vishnyakov, *Phys. Rev. E: Stat., Nonlinear, Soft Matter Phys.* **2000**, *62*, R1493.
- [71] L. D. Gelb, K. E. Gubbins, R. Radhakrishnan, M. Sliwinska-Bartkowiak, *Rep. Prog. Phys.* **1999**, *62*, 1573.
- [72] M. Thommes, R. Köhn, M. Fröba, *Appl. Surf. Sci.* **2002**, *196*, 239.
- [73] E. Barsotti, S. P. Tan, M. Piri, J.-H. Chen, *Langmuir* **2018**, *34*, 4473.
- [74] S. Dantas, K. C. Struckhoff, M. Thommes, A. V. Neimark, *Langmuir* **2019**, *35*, 11291.
- [75] M. Thommes, in *Annual Review of Nano Research*, World Scientific, **2009**, pp. 515–555.
- [76] A. V. Neimark, P. I. Ravikovitch, *Microporous Mesoporous Mater.* **2001**, *44*, 697.
- [77] P. C. Ball, R. Evans, *Langmuir* **1989**, *5*, 714.
- [78] K. Morishige, H. Fujii, M. Uga, D. Kinukawa, *Langmuir* **1997**, *13*, 3494.
- [79] C. G. V. Burgess, D. H. Everett, S. Nuttall, *Pure Appl. Chem.* **1989**, *61*, 1845.
- [80] A. de Keizer, T. Michalski, G. H. Findenegg, *Pure Appl. Chem.* **1991**, *63*, 1495.
- [81] J. A. Duffy, N. J. Wilkinson, H. M. Fretwell, M. A. Alam, R. Evans, *J. Phys.: Condens. Matter* **1995**, *7*, L713.
- [82] L. Sarkisov, P. A. Monson, *Langmuir* **2001**, *17*, 7600.
- [83] P. I. Ravikovitch, A. V. Neimark, *Langmuir* **2002**, *18*, 1550.
- [84] P. I. Ravikovitch, A. V. Neimark, *Langmuir* **2002**, *18*, 9830.
- [85] M. Thommes, B. Smarsly, M. Groenewolt, P. I. Ravikovitch, A. V. Neimark, *Langmuir* **2006**, *22*, 756.
- [86] C. J. Rasmussen, A. Vishnyakov, M. Thommes, B. M. Smarsly, F. Kleitz, A. V. Neimark, *Langmuir* **2010**, *26*, 10147.
- [87] M. Thommes, R. Köhn, M. Fröba, *J. Phys. Chem. B* **2000**, *104*, 7932.
- [88] K. A. Cychosz, X. Guo, W. Fan, R. Cimino, G. Yu. Gor, M. Tsapatsis, A. V. Neimark, M. Thommes, *Langmuir* **2012**, *28*, 12647.
- [89] K. Morishige, M. Tateishi, F. Hirose, K. Aramaki, *Langmuir* **2006**, *22*, 9220.
- [90] U. Müller, K. K. Unger, in *Studies in Surface Science and Catalysis*, Vol. 144, Elsevier, Amsterdam **1988**, p. 101.
- [91] P. L. Llewellyn, J. P. Coulomb, Y. Grillet, J. Patarin, H. Lauter, H. Reichert, J. Rouquerol, *Langmuir* **1993**, *9*, 1846.
- [92] K. Nakai, J. Sonoda, M. Yoshida, M. Hakuman, H. Naono, *Adsorption* **2007**, *13*, 351.
- [93] E. García-Pérez, J. B. Parra, C. O. Ania, D. Dubbeldam, T. J. H. Vlugt, J. M. Castillo, P. J. Merkling, S. Calero, *J. Phys. Chem. C* **2008**, *112*, 9976.
- [94] A. Galarneau, F. Villemot, J. Rodriguez, F. Fajula, B. Coasne, *Langmuir* **2014**, *30*, 13266.
- [95] A. V. Neimark, P. I. Ravikovitch, A. Vishnyakov, *J. Phys.: Condens. Matter* **2003**, *15*, 347.
- [96] M. Kruck, M. Jaroniec, A. Sayari, *Langmuir* **1997**, *13*, 6267.
- [97] M. Jaroniec, L. A. Solovyov, *Langmuir* **2006**, *22*, 6757.
- [98] G. Horváth, K. Kawazoe, *J. Chem. Eng. Jpn.* **1983**, *16*, 470.
- [99] A. Saito, H. C. Foley, *AIChE J.* **1991**, *37*, 429.
- [100] L. S. Cheng, Y. Ralph T, *Chem. Eng. Sci.* **1994**, *49*, 2599.
- [101] N. A. Seaton, J. P. R. B. Walton, N. quirke, *Carbon* **1989**, *27*, 853.
- [102] C. Lastoskie, K. E. Gubbins, N. Quirke, *J. Phys. Chem.* **1993**, *97*, 4786.
- [103] P. I. Ravikovitch, A. Vishnyakov, A. V. Neimark, *Phys. Rev. E: Stat., Nonlinear, Soft Matter Phys.* **2001**, *64*, 011602.
- [104] P. I. Ravikovitch, A. V. Neimark, *Colloids Surf., A* **2001**, *187*, 11.
- [105] X. Zhang, D. Liu, D. Xu, S. Asahina, K. A. Cychosz, K. V. Agrawal, Y. Al Wahedi, A. Bhan, S. Al Hashimi, O. Terasaki, M. Thommes, M. Tsapatsis, *Science* **2012**, *336*, 1684.
- [106] D. P. Serrano, J. Aguado, G. Morales, J. M. Rodríguez, A. Peral, M. Thommes, J. D. Epping, B. F. Chmelka, *Chem. Mater.* **2009**, *21*, 641.
- [107] J. P. Olivier, *Carbon* **1998**, *36*, 1469.
- [108] P. I. Ravikovitch, A. Vishnyakov, R. Russo, A. V. Neimark, *Langmuir* **2000**, *16*, 2311.
- [109] P. I. Ravikovitch, A. V. Neimark, *Langmuir* **2006**, *22*, 11171.
- [110] D. H. Everett, in *Solid-Gas Interface* (Ed: E. A. Flood) Dekker, New York **1967**, pp. 1055–1113.
- [111] R. Cimino, K. A. Cychosz, M. Thommes, A. V. Neimark, *Colloids Surf., A* **2013**, *437*, 76.
- [112] F. Kleitz, F. Bérubé, R. Guillet-Nicolas, C.-M. Yang, M. Thommes, *J. Phys. Chem. C* **2010**, *114*, 9344.
- [113] R. Guillet-Nicolas, F. Bérubé, M. Thommes, M. T. Janicke, F. Kleitz, *J. Phys. Chem. C* **2017**, *121*, 24505.
- [114] D. Schneider, R. Valiullin, *J. Phys. Chem. C* **2019**, *123*, 16239.
- [115] E. S. Kikkilides, P. A. Monson, R. Valiullin, *J. Phys. Chem. C* **2020**, *124*, 21591.
- [116] A. G. Khokhlov, R. R. Valiullin, M. A. Stepovich, J. Kärger, *Colloid J.* **2008**, *70*, 507.
- [117] H. Giesche, *Part. Part. Syst. Charact.* **2006**, *23*, 9.
- [118] J. C. Groen, L. A. A. Peffer, J. Pérez-Ramírez, in *Studies in Surface Science and Catalysis* (Eds: F. Rodriguez-Reinoso, B. McEnaney, J. Rouquerol, K. Unger), Elsevier, Amsterdam **2002**, p. 91.
- [119] F. Porcheron, P. A. Monson, *Langmuir* **2005**, *21*, 3179.
- [120] F. Porcheron, P. A. Monson, M. Thommes, in *Studies in Surface Science and Catalysis*, Vol. 160 (Eds: P. L. Llewellyn, F. Rodriguez-Reinoso, J. Rouquerol, N. Seaton, Elsevier, Amsterdam **2007**, p. 87.
- [121] L. Moscou, S. Lub, *Powder Technol.* **1981**, *29*, 45.
- [122] M. Hartmann, W. Schwieger, *Chem. Soc. Rev.* **2016**, *45*, 3311.
- [123] M. Thommes, R. Skudas, K. K. Unger, D. Lubda, *J. Chromatogr. A* **2008**, *1191*, 57.
- [124] M. Hartmann, A. Vinu, *Langmuir* **2002**, *18*, 8010.
- [125] A. Vinu, V. Murugesan, W. Böhlmann, M. Hartmann, *J. Phys. Chem. B* **2004**, *108*, 11496.
- [126] A. Galarneau, B. Lefèvre, H. Cambon, B. Coasne, S. Valange, Z. Gabelica, J.-P. Bellat, F. Di Renzo, *J. Phys. Chem. C* **2008**, *112*, 12921.



**Carola Schlumberger** studied Life Science Engineering at the Friedrich-Alexander-University Erlangen-Nürnberg. Since October 2019, she is working as a Ph.D. student at the Institute of Separation Science and Technology in Erlangen. During her Ph.D. studies, her focus is on combining gas adsorption with novel methodologies such as NMR relaxometry for reliable textural characterization and surface area assessment of porous materials.



**Matthias Thommes** obtained his Ph.D. in Physical Chemistry in 1993 at the TU-Berlin. From 1992 to 1995 he was a project scientist at the EURECA mission of the European Space Agency (ESA). In 1996, he moved as an ESA fellow/research associate to the University of Maryland, College Park, USA. In 1998, he joined Quantachrome Corp. and held from 2001 to 2018 the position of scientific director (Boynton Beach, FL, USA). Since 2018 he is professor and head of the Institute for Separation Science and Technology at the University Erlangen-Nürnberg. In addition he holds the position of visiting professor at the University of Edinburgh (since 2012), UK and Lorraine University, Nancy, France (since 2017).